Distinguishing different radioactive sources with operative plastic scintillators

Master's Thesis, 23.5.2018

Author:

OLLI VIRKKI

Supervisors:

KARI PERÄJÄRVI
FINNISH RADIATION AND NUCLEAR SAFETY AUTHORITY, STUK

ARI JOKINEN
DEPARTMENT OF PHYSICS, UNIVERSITY OF JYVÄSKYLÄ

UNIVERSITY OF JYVÄSKYLÄ
JYVÄSKYLÄN YLIOPISTO

STUK

Abstract

Virkki, Olli
Distinguishing different radioactive sources with operative plastic scintillators
Master's Thesis
Department of Physics, University of Jyväskylä, 2018, 80 pages

Plastic scintillators (PS) are widely used as radiation monitors in industry and border control. Besides being a fast scintillation material, the low material cost, efficient bulk production and high sensitivity due to big sizes have made PSs a foundation of most radiation monitors as they are fast and cheap to deploy and efficient detectors. Due to their limited capabilities to distinguish different radiation sources, in the past they were mainly used as rough counters only to detect radiation. The increasing demand for different radioactive materials in industry and medical field increase the risk of illicit and inadvertent use or radiation sources. As a counterpart, the abundant naturally occurring radioactive materials (NORMs) in most cases do not require further investigation. Minimizing unnecessary workload while keeping the radiation monitoring efficient gives rise to the need of radiation source identification methods.

The goal of this Master's thesis is to offer insight for plastic scintillators from an operational viewpoint. Possible next-generation operation modes for more precise radiation monitoring as well as different characterization methods to probe the functionality of a plastic scintillator are presented and tested in practice. The methods can be executed in on-field conditions and are applicable for plastic and other scintillation materials used in both operational and laboratory purposes.

Keywords: Plastic scintillator, Radiation monitoring, Scintillator characterization

Tiivistelmä

Virkki, Olli
Säteilylähteiden tunnistaminen operatiivisilla tuikeilmaisimilla
Pro-gradu tutkielma
Fysiikan laitos, Jyväskylän Yliopisto, 2018, 80 sivua

Muovisia tuikeilmaisimia käytetään laajasti säteilyvalvonnassa sekä teollisuudessa että rajavalvonnassa. Niiden suhteellisen matalat materiaalikustannukset, massatuotantokyky, tuikemateriaalin nopeus sekä suuret koot mahdollistavat nopean käyttöönoton ja korkeat havaitsemistehokkuudet. Tämän takia niitä käytetään lähes jokaisella säteilymonitorointiasemalla. Muovisilla tuikeilmaisimilla on vaikeuksia tunnistaa eri säteilylähteitä, jonka takia niitä on käytetty aiemmin pääasiassa säteilyä havaitsevina laskureina. Teollisuudessa ja lääketieteessä käytettävien säteilylähteiden kysynnän kasvaessa riski säteilylähteiden sopimattomaan ja huolimattomaan käyttöön kasvaa. Normaalissa liikenteessä kulkee myös paljon luonnon radioaktiivisia aineita (NORM) sisältäviä lähteitä, jotka eivät vaadi tutkinnallisia jatkotoimenpiteitä. Jotta ylimääräinen työ saataisiin minimoitua kuitenkin pitäen säteilyvalvonnan taso korkealla, säteilylähdetunnistusta on tutkittu ja sovellettu muovisillekin tuikeilmaisimille.

Tämä pro-gradu tutkielma pyrkii avartamaan muovisten tuikeilmaisimien toimintaa operatiivisesta näkökulmasta. Tutkielmassa esitellään ja kokeillaan käytännössä nukliditunnistusta edistäviä analysointeja sekä erilaisia karakterisointimenetelmiä muovin toimintakyvyn tarkastelemiseksi. Nämä metodit voidaan suorittaa kenttäolosuhteissa ja on sovellettavissa muovisiin ja muunlaisiin tuikeilmaisimiin kentällä ja laboratoriossa.

Avainsanat: Muovinen tuikeilmaisin, säteilyvalvonta, tuikeilmaisimien karakterisointi

Preface

In Tuusula at May 23$^{\text{rd}}$, 2018

Olli Virkki

Contents

List of Figures

List of Tables

1   Introduction

Efficient monitoring of the flow and movement of nuclear and other radioactive materials is a vital point in maintaining national security. With an increase of various users of radioactive materials – e.g. in nuclear power, medical field and industry – the risk of improper handling of artificial radionuclei becomes relevant. The legal flow of radioactive materials has also grown accordingly. In a mission to maintain the national security customs have a vast arsenal of radiation detectors for vehicle and pedestrian scanning at border crossing points. The primal inspection stations are typically stationary plastic based radiation portal monitors.

These monitors are usually positioned on the side of the lanes to scan vehicles and pedestrians in a fast rate and their task is to give an alarm in case they detect radioactive substances and materials. Plastic scintillators (PS) are usually selected for this task because they are a fast material, and for their efficient bulk production, high sensitivity due to their achievable large sizes, and cheap material costs. The main limitation of PS is poor energy resolution, i.e. the ability to distinguish different radiation energies, which challenges the source identification methods.

When using PSs only as rough counters, a big portion of radiation alarms are so called nuisance alarms. These are real alarms caused by naturally occurring radioactive materials (NORMs) e.g. natural uranium or thorium in porcelain and construction aggregates. Because a moderate amount of NORM substances are allowed the further inspection processes of NORM containing loads is in most cases unnecessary. Specialized algorithms are therefore needed to distinguish NORM loads, forcing the limited resolution of a PS to be utilized.

As a secondary motivation for this thesis, the lifespan of a PS is roughly 10 years. During its lifetime PS's detectability decreases and requires recalibration and eventually replacement. Furthermore, it has been shown [1] that different PSs age independently which allows the replacement of individual radiation monitors over a wide timespan. To continue PSs operation over the the expected replacement date will also save expenses especially since plastic based radiation monitors are usually part of large scale systems[1].

---

[1]As of October 2016 there was 1400 radiation portal monitors stationed in United States of America most of them containing 4 PSs [9].

2   Theoretical background

2.1   Photon interactions in plastic

As a gamma ray interacts with scintillation material secondary photons are emitted. The most probable type of interaction depends on the energy of the incident gamma and the mass number of scintillation material as shown in Fig. 1. For our purposes we concentrate on low-Z region as the plastic scintillators are mainly hydrocarbons. For $Z < 20$ the Compton effect is dominant at the energy range of 100 keV – 10 MeV, which covers almost the whole range of gamma radiation from common radioactive nuclei, missing out only the lowest energies [2]. Pair production is highly improbable in our energy range of interest and thus not discussed from this point onwards.

The probability coefficient τ for photoelectric absorption is proportional to $Z^n/E^{3.5}$ [6, p. 49], where Z is the mass number of the absorber, n is a constant between 4 and 5 and E is the energy of the incident photon. This model of τ creates a straight descending line in log-log scale when plotted as a function of energy E. We can observe this from the behaviour of mass attenuation coefficient μ/ρ graph of a common scintillation material vinyl toluene shown in Fig. 2. The attenuation coefficient μ is the sum of the probabilities from photoelectric absorption, Compton scattering and pair production, and ρ is the medium's density. Because the linear region of the graph changes significantly at roughly 50 keV and according to the model the component of the photoelectric absorption becomes very small, we can assume that all the interactions undergone by photons in the scintillation material is via the Compton scattering. It is worth mentioning here that μ is also the reciprocal of attenuation length λ which describes the distance a gamma beam has to propagate within the medium for its intensity to drop to one e'th.

---

[2]The highest gamma energies considered in this thesis is 4.4 MeV from α-Be neutron source and fission gammas up to 5 MeV.
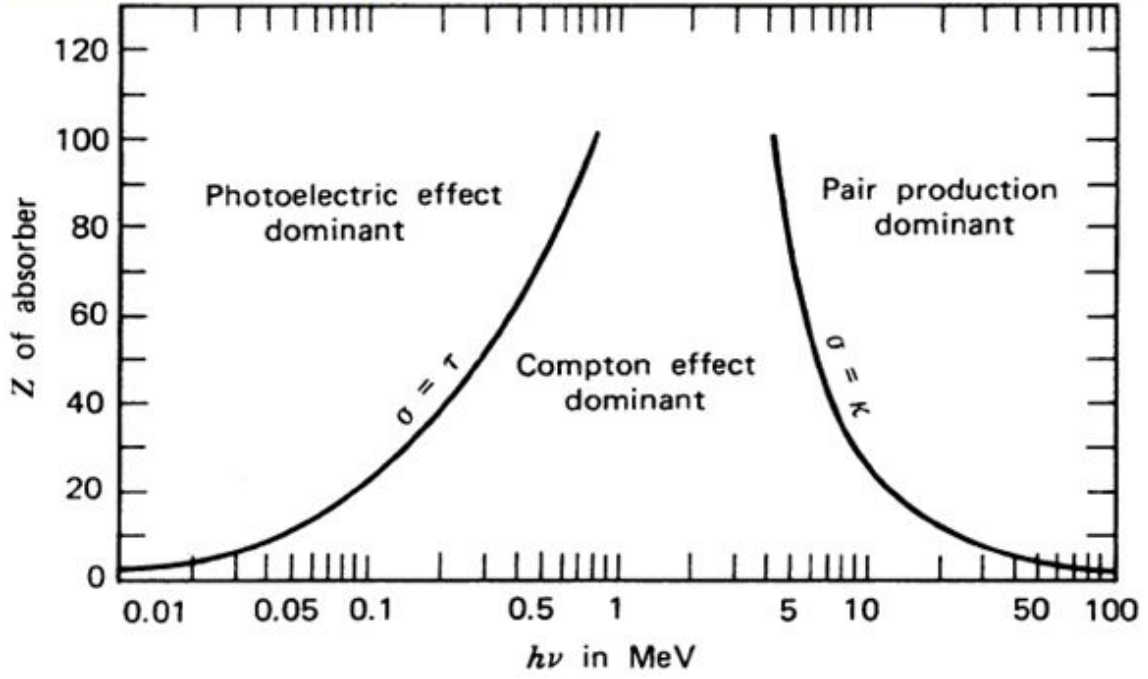
Figure 1. Probability scheme for different gamma scattering interaction probabilities showing equality borders where the probability of neighbouring interactions are equal. Figure from Ref. [6].
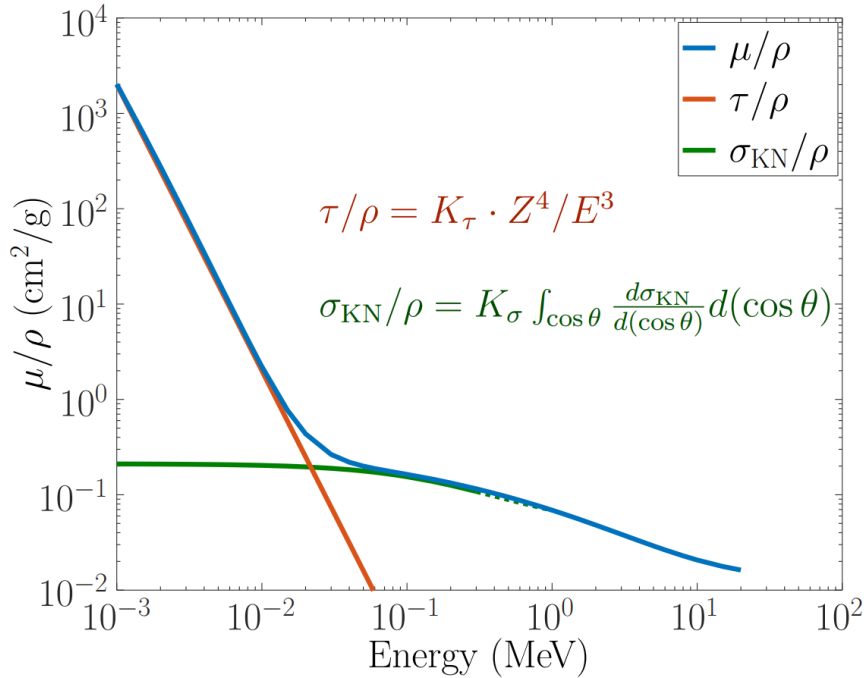
Figure 2. Mass attenuation coefficient data μ/ρ for vinyl toluene and modelled photoelectric τ/ρ and Compton scattering σ_{KN}/ρ components. K_i are scaling constants and $d\sigma_{KN}/d(\cos\theta)$ the Klein-Nishina formula [6]. Data from Ref. [10].

2.2 Compton scattering

In Compton scattering part of the initial gamma's energy E is transferred to the scattered electron according to equation

$$E^* = \frac{E}{1 + \frac{E}{m_e c^2}(1 - \cos\theta)} \tag{1}$$

where E^* is the energy of the scattered gamma, $m_e c^2$ the rest mass of an electron and θ is the gamma's scattering angle. The rest of the energy, $T = E - E^*$, is transferred to the electron from which the gamma scattered. The Compton scattering process is illustrated in Fig. 3.

The probabilities for each scattering angles are not equally distributed. The differential cross section for an initial gamma of an energy E to scatter in an angle θ, per atom, is given by the Klein-Nishina formula

$$\frac{d\sigma_{\mathrm{KN}}}{d\Omega} = Zr_0^2 \left(\frac{E^*}{E}\right)^2 \left[\frac{E^*}{E} + \frac{E}{E^*} - \sin^2(\theta)\right] / 2 \tag{2}$$

where $d\sigma_{\mathrm{KN}}/d\Omega$ is the differential cross section for a scattering angle element, Z the number of electrons per atoms (or the atomic number of the absorber material), r_0 the classical electron radius, and E^* the photon's energy after the scattering as given by Eq. (1). For a free electron $Z = 1$.

When the energy transferred to the scattered electron T is of interest, such as in case of scintillators, one can use the reformed Klein-Nishina formula

$$\frac{d\sigma_{\mathrm{KN}}}{dT} = \frac{Zr_0^2 \pi}{m_e c^2} \cdot \frac{1}{\alpha} \left(2 + \frac{S^2}{\alpha^2(1-S)^2} + \frac{S}{1-S}\left(S - \frac{2}{\alpha}\right)\right) \tag{3}$$

where $\alpha = E/m_e c^2$, and $S = T/E$. This differential cross-section is directly proportional to the probability distribution for the scattered electron to have kinetic energy T.

For a derivation of equations (2) and (3) see Appendix A.1.

As the scattered gamma's energy reaches its minimum at a 180° backscattering, the maximum values for T and S are

$$T_{max} = E - E^*_{min} = E - E\frac{1}{1 + 2\alpha} = E\frac{2\alpha}{1 + 2\alpha} = m_e c^2 \frac{2\alpha^2}{1 + 2\alpha} \tag{4}$$

and

$$S_{max} = T_{max}/E = \frac{2\alpha}{1 + 2\alpha}. \tag{5}$$

The energy T_{max} is called as Compton edge energy and corresponds to the highest energy deposited by a photon in Compton scattering.
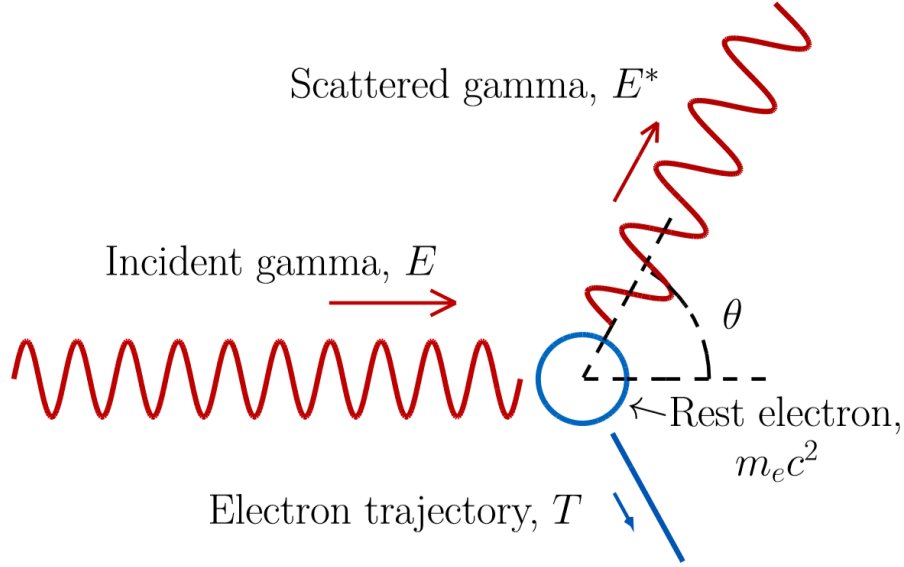
Figure 3. Illustration of the Compton scattering process.

2.3 Scintillation and energy level structure in plastic

The Compton scattered electron will eventually interact with other electrons of the scintillation material creating molecular excitations. As these excited states return to ground level so called secondary or scintillation photons are emitted. In some cases the secondary photon is of the same energy required to excite the molecule resulting into so called self-absorption. For a photon to propagate within the scintillation material these scintillation photons must have a lower energy. In organic scintillators this is acquired by the molecules' energy structure.

To minimize this self-absorption in plastic and other organic scintillation materials the molecular energy level structure with so called π-orbitals are of interest. An energy level scheme for these orbitals are shown in Fig. 4. The energy levels are indexed as $S_{i,j}$, where i corresponds to the excitation level and j its vibrational sublevel. When the electron is excited to some non-zero vibrational level of an excitation state (say, $S_{1,1}$), it quickly loses the vibrational energy in the form of heat and moves to the zero vibrational state of that excited state ($S_{1,0}$) in the matter of picoseconds. From here the electron can decay into any vibrational states ($\sim 10^{-8}$ s) of the lower energy levels (e.g. $S_{0,1}$) emitting a secondary photon. This vibrational state again quickly decays into zero-vibrational state ($S_{0,0}$). [6]

For the sake of completeness, the molecule can also excite into triplet states. Because their lifetime is much longer ($> 10^{-4}$ s) and as the time window of one gamma interaction is of the order of $100 - 1000$ ns (discussed further in section 3.2) the triplet states do not contribute to our measurements and are thus ignored.

The benefit of the π-structure is that the emitted photon does not have enough energy for self-absorption if the decay happened via a vibration state. Therefore
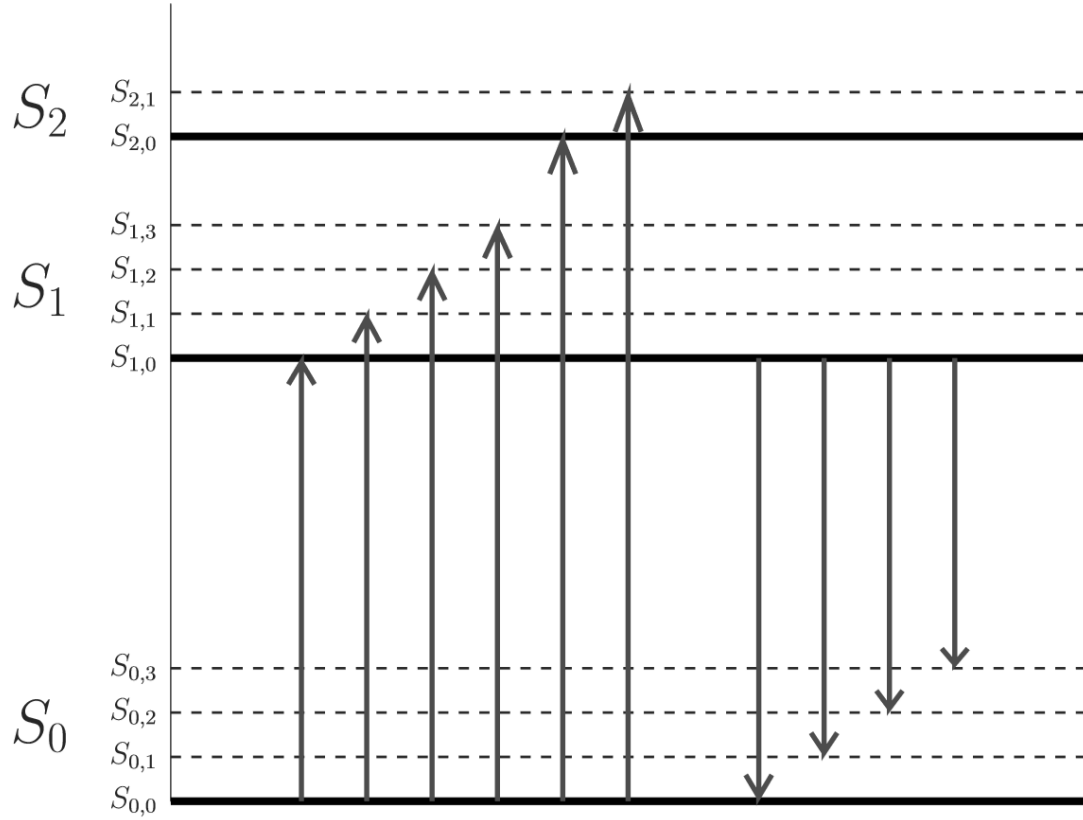
Figure 4. π-structure of energy levels in organic molecule.

the emission spectrum gets shifted towards longer wavelengths with respect to the absorption spectrum. This is commonly called a Stokes shift.

The Stokes shift of the base material, or solvant, alone is usually not enough and is enhanced with different dopants to further minimize self-absorption. Different dopands are chosen according to desired applications for the material. Some common dopants are p-terphenyl, PPO and POPOP. The overlapping of absorption and emission spectra of some commercial polyvinyl toluene (PVT) based scintillators can be observed in Fig. 5. While the base material is the same (PVT) the dopants affect greatly to the optical spectra.
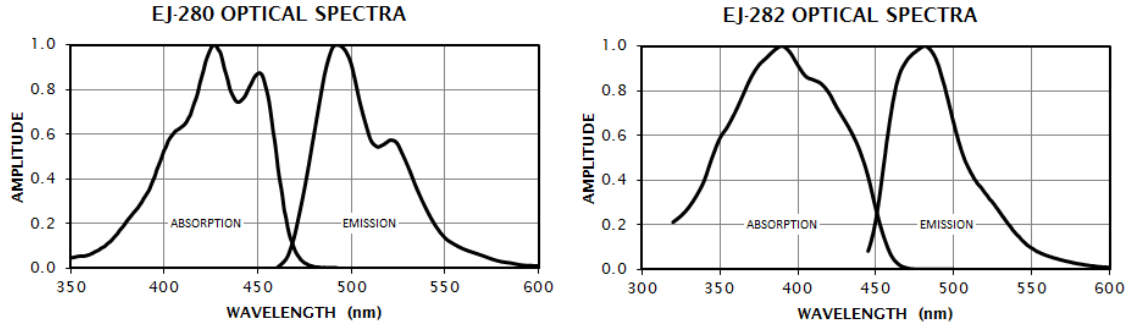
Figure 5. Absorption and emission spectra of polyvinyl toluene based wavelength shifters. Figure from Ref. [16].

2.4 Radioactive sources

After a nucleus has undergone a decay or has been created in a nuclear reactions, the daughter nucleus can be in excited states. Given that no further processes were undergone, these states further decay into lower excited states and eventually to their ground states. During these processes gamma radiation is emitted which are characteristic to each nuclei. Detecting the characteristic gammas is in most cases the main identification method.

While not relevant in this thesis, fission sources and β-emitters also radiate gammas. In fission the daughter nuclei can have varying kinetic energies and the prompt gammas emitted have a continuous energy spectrum. Electrons from β-emitters, most notably ^{90}Sr and ^{90}Y, also create a continuous gamma spectrum as they travel in a medium via bremsstrahlung.

There is a variety of radioactive sources. ^{241}Am is a very common calibration source for it decays only via α-decay and mainly (84.6%) into an excited state of ^{237}Np with an energy of 59.5 keV. While ^{241}Am has a half life of 432 years, the lifetime of the excited state of ^{237}Np is only 67 ns. Because the lifetime of ^{237}Np is of the order of 10^6 years the 59.5 keV is the dominant gamma radiation energy of an ^{241}Am source. Another common source, ^{137}Cs, β-decays into ground state or an isomeric level of ^{137}Ba with an energy of 661 keV. Some sources, including ^{241}Am, decay further and thus emit multiple gammas with different energies. One of the longest common decay chain starting from the NORM ^{238}U has 14 steps before reaching the stable ^{206}Pb where most of the steps emit gammas, including the 2614 keV gamma from the decay of ^{208}Tl. Because the lifetimes of the intermediate nuclei in this so called uranium series vary from 10^5 years to few seconds, the ^{238}U-source has a high number of characteristic gammas. Lastly, a beryllium-based neutron emitters such as ^{241}AmBe undergoe a fusion process ^{9}Be$(\alpha,$n$)^{12}$C where the created carbon nucleus can be at its excited state of 4.4 MeV. [15, 8]

Most of the gamma energies from radioactive sources of our interest fall between the 59.5 keV from ^{241}Am and 2614 keV one from ^{208}Tl. Some other radiation sources

are also used to get intermediate gamma energies, where most important to this thesis are ^{133}Ba (356 keV), ^{137}Cs (661 keV), ^{60}Co (1173 keV and 1333 keV) and the important NORM, ^{40}K (1460 keV).

3   Scintillator system

In this section the scintillator hardware used in our measurements is described. Because the signal processing setup varies between measurements the complete setup with the modules used are described individually in each section. All hardware and software are also listed at the end of the Reference section.

3.1   Scintillation material

The plastic scintillator shown in Fig. 6 is used in our measurements and is from a commercial radiation monitor. This unit is roughly ten years old and has been in operational use in an environment with rough weather conditions including high humidity and temperatures varying from -30°C to +30°C annually. The scintillator casing was never opened and is assumed that the scintillator material was wrapped in a reflective foil and then to a black plastic wrapping. The scintillator material is assumed to be polyvinyl toluene (PVT) which is the base material in most common plastic scintillators. Different plastic scintillation materials vary mainly in operative appliances, decay time, luminescence, sensitivity and absorption-emission spectra, all of which do not affect our measurement methods and results significantly. All common plastic scintillation materials also fulfil the requirements and assumptions made in this thesis. Properties of common plastic scintillation materials are shown in Table 1. As mentioned earlier, the attenuation length is the distance after which the light's intensity has dropped to one e'th.

Table 1. Properties of some commercially available plastic scintillators [16, 12]

Name	Base	Density (g/cm^3)	Refractive index	Decay constant (ns)	Emission Max. wavelength (nm)	Attenuation length λ (cm)
EJ-200	PVT	1.023	1.58	2.1	425	380
EJ-204	PVT	1.023	1.58	1.8	408	160
EJ-208	PVT	1.023	1.58	3.3	435	400
IHEP – SC-201 – SC-205	PS	1.05	1.59	3.0	420	200

PVT= polyvinyl toluene, PS = polystyrene
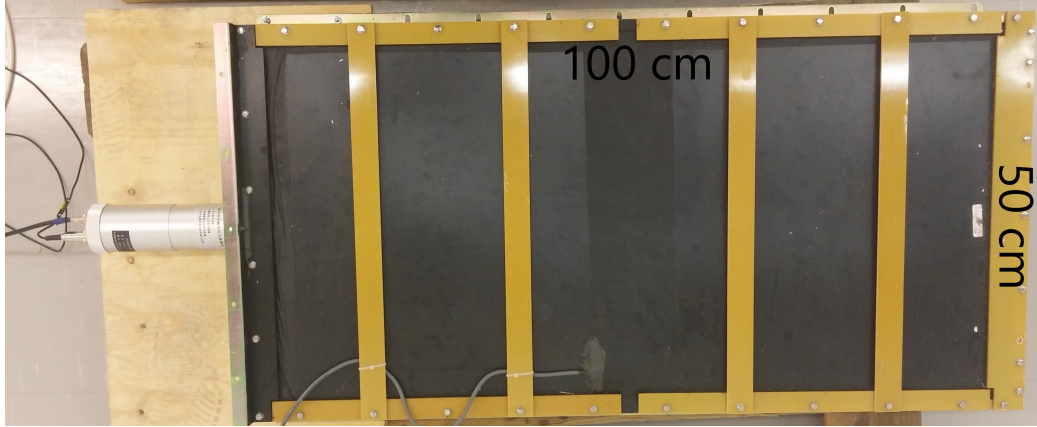
Figure 6. The top view of the plastic scintillator mainly used for our measurements

3.2 Photomultiplier tube

The secondary photons emitted via scintillation propagate eventually to a photomultiplier tube (PMT). PMT consists of three main components: a photocathode, a dynode line and an anode. The working principle is illustrated in Fig. 7. When a photon hits the photocathode of the PMT, a photoelectron gets released. This electron is then led through a series of dynodes each in a higher potential than the previous one. Upon impacting a dynode an electron can release additional electrons from it multiplying the number of electrons accelerated towards the next dynode. This creates a avalanche of electrons all which eventually reach the last dynode named anode. The current reaching anode creates a signal which is fed to the signal processing unit.

In practice PMT has some capacitance since the anode gets charged during a period of time to discharge afterwards. Like for all capacitors, the time constant varies by unit, but in this thesis the time during which the charge decays from the maximum to one e'th is the order of $100 - 1000$ ns.

The scintillator material block is connected to a PMT-preamplifier combo (PP) with optical grease without additional light guide. For each scintillation event the PP gives a voltage pulse of negative polarity with an amplitude ranging from -10 mV to -2 V. An amplitude of -100 mV corresponds roughly to 530 keV. A general shape of this signal is shown in Fig. 8. The signal has a width of few hundreds of nanoseconds as described earlier depending on the amplitude of the signal. The PP is cased in a metallic cylinder which is visible at the left end of the scintillator shown in Fig. 6.
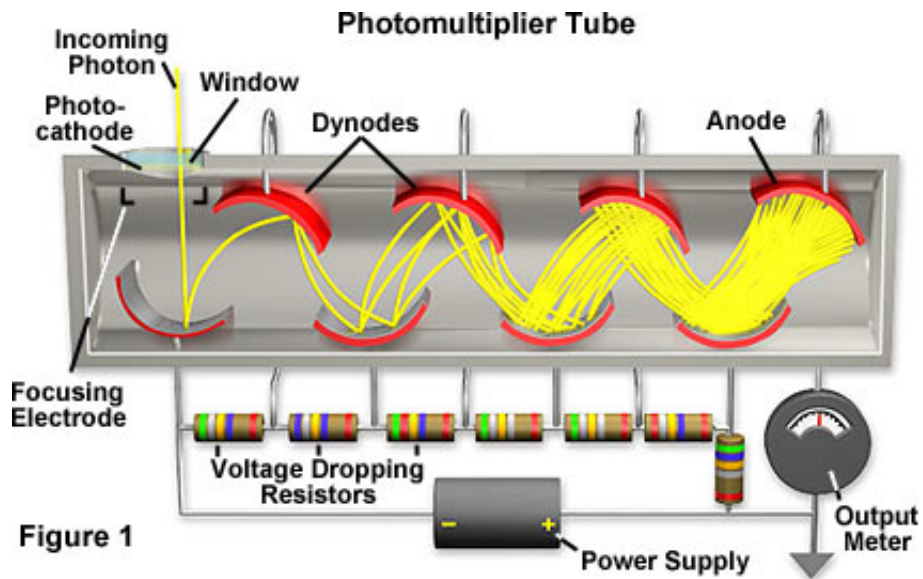
Figure 7. Illustration of the working mechanism of a PMT. Figure from `hamamatsu.magnet.fsu.edu`.
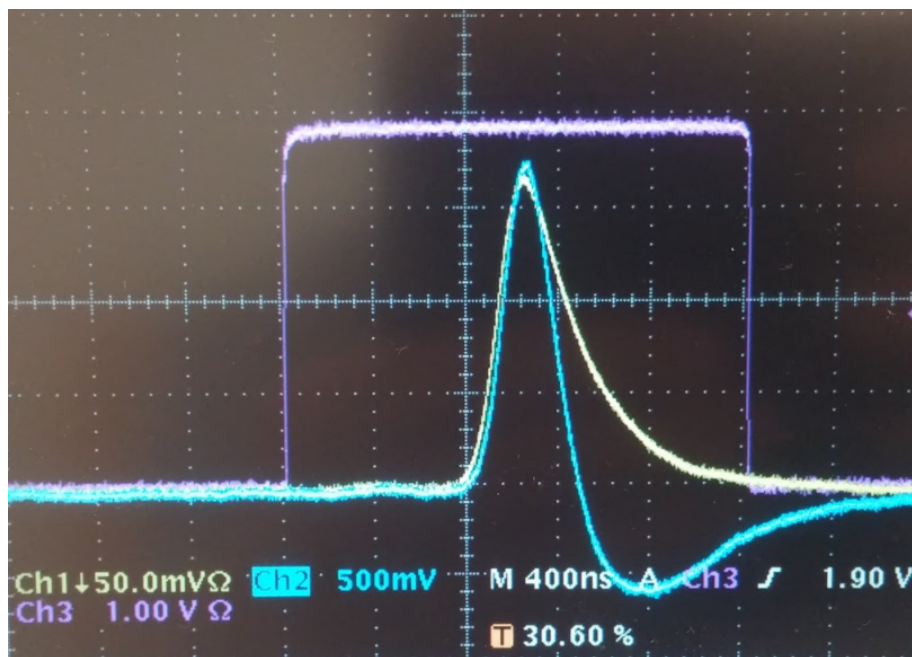
Figure 8. Generic signal produced by the PMT-premaplifier combo viewed by an oscillator. Yellow: the original signal inverted. Blue: amplified signal with -10x gain by a time filtering amplifier. Purple: gate signal used in Section 5.2.

4 Operative usage

In the past, plastic scintillators were mainly used as rough counters to detect a presence of a radioactive source. The alarms resulting from NORMs, sometimes referred to as nuisance alarms, are very frequent due to the high abundance in shipped cargo. While the radiation is indeed present, in most cases it does not exceed the allowed concentration or strength limits creating unnecessary work for the inspection personnel. This is one of the reasons why better resolution devices, such as sodium iodine (NaI) detectors, have gained popularity in order to distinguish the NORM loads. Still, plastic scintillators can be set up to give a rough estimate of the radioactive sources. Usually this is done by dividing the signals into bins according to their amplitudes. This is called energy windowing as the signal amplitude is proportional to the energy disposed to the PS by the initial photon. Increasing the number of energy windows eventually leads to spectroscopy but using only few energy windows keeps the system simple and robust. We will study the advantages and disadvantages of the two channel method, and suggest ways for measurement analysis.

4.1 Two-channel method (2C)

Artificially made radioactive nuclei radiate mainly at low energies, whereas the lowest gamma energy for NORMs used for nuclide identification is 1460 keV photopeak from ^{40}K. This allows us to make a simple estimation, stating that as long as a source radiates only gammas with energies below 1460 keV, it is artificial or otherwise worth investigating. This statement is very straightforward to implement to the hardware while allowing flexibility between individual radiation monitors.

While the Compton scattering from the PS creates a range of energies that are read as pulse signals, each gamma can transfer a maximum of an 180° backscattering. Since the signal from PMT is proportional to the energy transferred to PS one only needs to probe whether a present source creates signals above a certain reference signal or not.

4.1.1 2C: Working principle

The signal processing can ultimately be done by dividing the voltage signal from PMT with two comparators. The reference voltage of the first comparator, V_1, should be set low only to cut off the electric noise. The reference voltage of the second comparator, V_2 where $V_2 > V_1$, is used to divide the bins. The outputs are then led to individual pulse counters.

For the sake of simplicity, since signals over V_2 are passed by both comparators, one should make the counters anti-coincide with each other. This can be done by either subtracting the counts of higher window from lower window or by implementing logical gates. As a result, the first counter only detects signals between voltages V_1 and V_2 and the second counter detects signals over V_2. The second counter was left without an upper limit.

Because the lower voltages correspond to lower gamma energies, we will herein call the first counter the LOW channel. Similarly, the second counter is called the HIGH channel. The term channel is used for convenience as it is more commonly used when the number of energy windows increase.

A HIGH/LOW ratio (or its reciprocal) has been discussed in early literature [2] but it has a tendency to miss out information. As the radiation source becomes stronger the count rates start to skew towards HIGH channel due to the limited resolution of PS. Therefore the concept of total count rate, HIGH+LOW, has to be induced to the model as well. Further, if the source is weak compared to the background the ratio does not change significantly. The debatable improvement of background subtraction in this case could result in division by zero.

Our analysing method presents the count rates in a simple double logarithmic graph where the HIGH (LOW) channel count rate is on x(y)-axis. This provides a quick visual of the measurement results while maintaining the contrast to the background. It uses the advantage of the unique spectra created by different radiation sources and the changes in count rates as the strength of the source relative to the detector changes.

4.1.2 2C: Measurements and results

The first task is to calibrate the reference voltages V_1 and V_2. This can be done using ^{241}Am and ^{137}Cs sources as they are very common industrial sources and have a relatively long lifetime. The lower threshold, V_1, should be calibrated to reduce the electric noise as much as possible while still passing through most of the signals created by ^{241}Am source. One should also note that below the 59.5 keV gamma of ^{241}Am lies some common radiation sources, such as 35.5 keV from medical ^{125}I ($T_{1/2} = 60$ days). The voltage V_2 should utilized to distinguish NORM sources. A prominent location is to set it high while maintaining the visibility opf ^{40}K.

In our setup the spectra of different radiation sources were measured with PS. The signal from PP is fed via an inverter (Philips Scientific, model 740) to a multichannel analyzer (MCA, Ortec 927) which is connected to a computer with appropriate software. We simulated the HIGH and LOW channels by integrating the count rate along specific channel ranges. This is justified because a channel in MCA spectrum is linearly proportional to a specific voltage amplitude range in PMT. Using an MCA allows us also to create a visual picture of where the reference voltages are located in the energy spectrum.

The key points in the calibration process are to first maintain the detectability of low energy source and to distinguish ^{40}K and ^{60}Co sources as they have very similar energies. ^{133}Ba with a 356 keV photopeak was used as a low energy source in our calibration. The channel ranges for LOW and HIGH energy windows were selected to be channels 18 and 80, and because the MCA was operated in 4096 channel mode with voltage range from 0 V to +10 V, the corresponding reference voltages are 44 mV and 195 mV, respectively. The radiation sources used in the experiment were measured from multiple distances ranging from 9 cm to 300 cm depending on the source to simulate different intensity sources. Additional amplifiers were not used as the ones available had a tendency to induce artefacts during the experimenting phase.

The resulting HIGH-LOW graph is shown in Fig. 9 and some of the the MCA spectra with the used channel limits in Fig. 10. The most visible anomaly in Fig. 9 is the location of ^{133}Ba data points. A closer inspection in the spectrum graph (Fig. 10) reveals that the decrease of count rate with respect to background in HIGH channel is mainly due to the statistical error near channels 80–100. This is a great visual hint of the uncertainty region around the background in which an increase in either channel can and should be considered to be within the noise region. The leaning towards the HIGH channel can be seen from the ^{137}Cs and natural uranium (NU) plots as well as higher energy sources (e.g. ^{152}Eu, not shown completely).

Each radiation source has a characteristic HIGH/LOW ratio and the stronger the source is the further it is from the background point. Varying the intensity creates paths, source lines, in the HIGH-LOW graph. These lines may vary depending on the casing shielding the radiation monitor. By inserting a small margins one can create regions for each source denoting the corresponding source's data region. Changing the channel dividing point (grey lines in Fig. 10) will result in changes of source lines in Fig. 9 which allows one to manipulate the proximities of source lines. As an example, for NORM identification the ^{40}K and ^{232}Th sources will be treated the same which makes their source line overlap insignificant. In turn, the overlap between ^{40}K and ^{60}Co should be minimized as ^{60}Co is an industrial source, which requires further investigation.

Even while the energy calibration will be different for each PS, if one desires to create a HIGH-LOW calibration for multiple plastic radiation monitors with identical setup referring a calibration spectra should be sufficient instead of measuring all
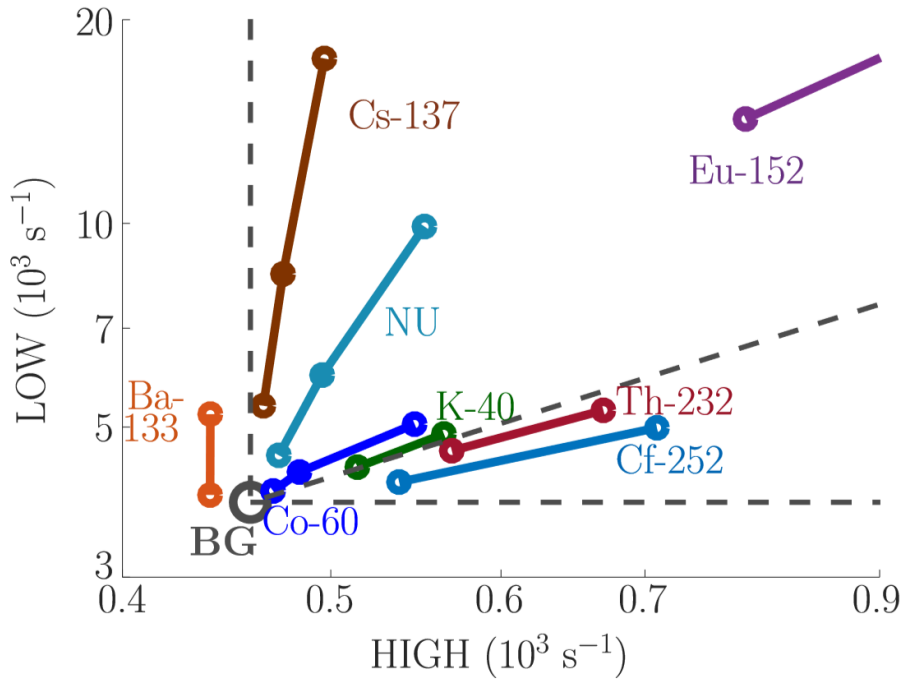
Figure 9. HIGH-LOW graph formed by 2-channel method. The dashed lines box the background region and show a linear reference line passing through the origin and background data point.
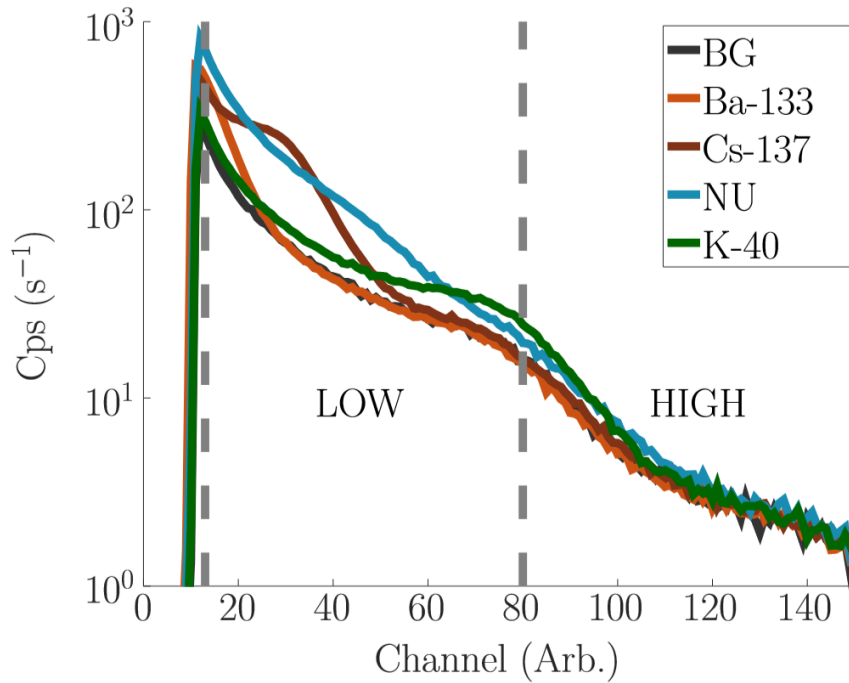
Figure 10. Some of the spectra used for the channel analysis. The grey dashed lines show the location of energy window dividing channels.

sources with all PS. A reference spectrum can be a background spectrum as long as the shape of the background spectra are the same, or alternatively a background subtracted ^{137}Cs spectrum. The difference in the energy resolutions – the capability to distinguish different gamma energies – between multiple PS can be speculated to affect mainly the leanness of the source lines as the intensity of the source increases.

It is noteworthy that the counts from the low-end of an energy window dominate the high end counts. Considering the ^{40}K spectrum in Fig. 10, the ratio between ^{40}K count rate and background count rate are 1.11 and 1.27 at channels 20 and 70, respectively. Moving the lower limit of LOW window to higher channels will thus enhance the visibility of a ^{40}K source. This is because the count rate is higher at lower channels but has smaller significance for ^{40}K. Dividing the energy windows to smaller sub-windows directly enhances the detectability since the significance of count rate increase along the whole energy region becomes more equal[3].

4.2 Channel detectability enhancement

When measuring traffic with the radiation monitor, the signal from PS is fed to comparators and the number of counts from both comparators within a fixed time interval is recorded. The reciprocal of this recording time is called the sample rate. While the high processing speed of PS allows high sample rates up to the order of 100 Hz, decreasing the sample rate reduces the fluctuations in the count rates. As a drawback, with low sample rates the overall detectability decreases for fast passing sources. Varying velocities of passing vehicles demands play with the sample rates for individual radiation monitoring system. A simulated illustration of this effect is shown in Fig. 11 where the passing source is represented by a Gaussian shape with added white noise.

The detectability can be enhanced also by understanding that the change of count rate due to a moving radiation source is well-behaving. While the fluctuations are well visible in high sample rates (the 1000 Hz line in Fig. 11) the count rate does increase on average when a source is present. Therefore by analysing the progression of the mean we can detect the signal induced increase in our count rate graph. This moving mean graph is done by plotting the mean of all counts within an expanded time interval for all sample points as the mean location [4]. An illustrating graph from the simulation above is presented in Fig. 12.

---

[3]Increase of the count rate by 10 cps has higher significance the lower the background is.

[4]This is a convolution between the data and a rectangular function.
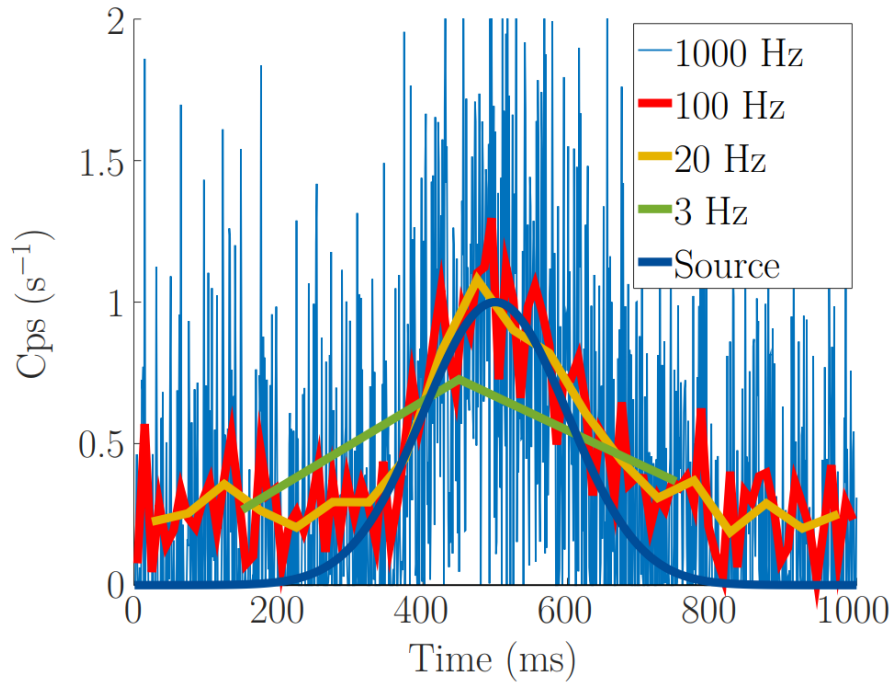
Figure 11. Illustration of the effects of different sample rates.
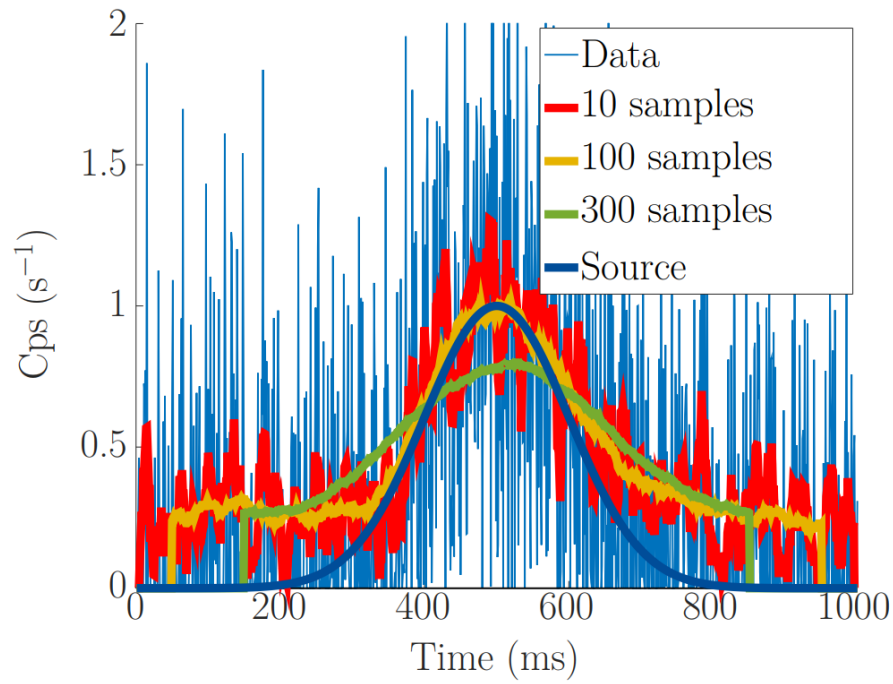
Figure 12. The mean for each mean location with different sample intervals.

4.3   Practical appliance

A PS similar to this thesis' was positioned next to a road with vehicle traffic. In our setup the sample rate was set to 20 Hz with a 20 sample (1 second) mean span. Stationary radiation sources were first measured in order to achieve a proper calibration. In the lack of a feasible ^{40}K source the V_2 is set just above the limit where the ^{137}Cs source becomes visible, so that the voltage should correspond to roughly 600–800 keV. After calibrations an unknown source was measured. The background was also measured individually for all measurement set right before measuring the source.

The resulting HIGH-LOW graphs for the sources are shown in Fig. 13 and the moving mean graph with a 1 second interval in Fig. 14. All data has been offset so that the background data points become equal for the sake of source comparison. This can be done as the background can be arbitrary as long as it is well known, while the count rate increase from a stationary source is constant[5]. The ^{133}Ba source being directly above the background is a strong industrial source indication, but has big fluctuations in the HIGH channels probably due to background. Data from ^{137}Cs, ^{60}Co and unknown sources can be easily divided with linear lines and after consulting Fig. 9 the unknown source can be declared as a moving ^{40}K source. Because we did not measure ^{40}K systematically, the declaration requires further experimenting to locate source lines and regions.

During a radiation alarm the graphs in Fig. 14 can provide a quick insight for types of radiation sources present. Most importantly, separating NORM sources allows different procedures and reduces nuisance alarms. The alarm levels can be ultimately defined with the background level and the regions to which the source lines get drawn.

A measurement of a vehicle without a radiation source is shown in Fig. 15. The background's count rate visibly decreases as the vehicle passes the radiation monitor. This is due to the vehicle blocking some of the background radiation that would otherwise be detected by PS. This effect, commonly called "vehicle shielding", should be taken into consideration when setting up vehicle radiation monitor systems and especially the alarm algorithms.

---

[5]The background level does affect the statistical detection sensibility and is relevant when considering alarm levels
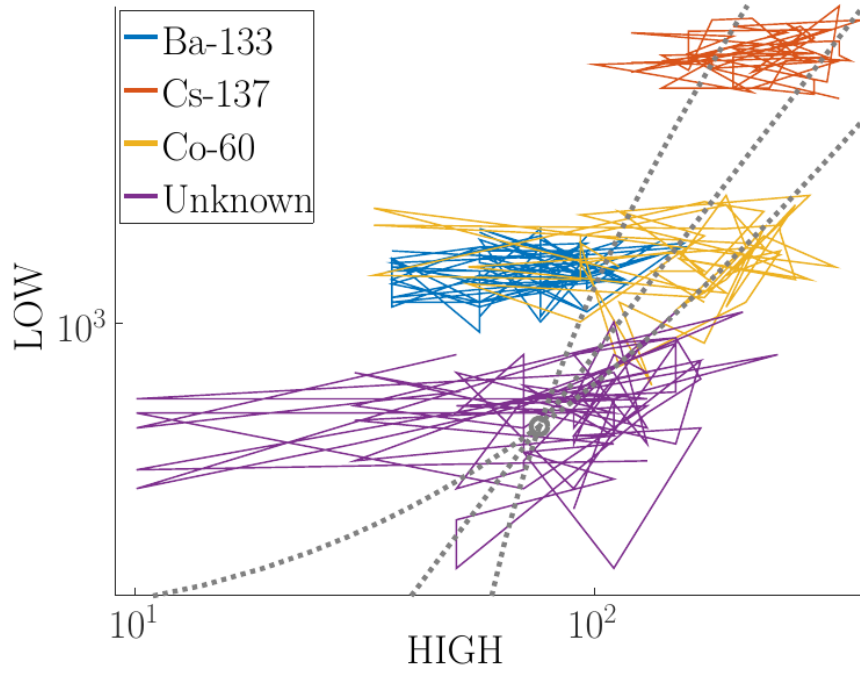
Figure 13. Different radiation sources measured with the PS using 2-channel method. All data is offset for a single background point (grey circle). Grey dashed lines are linear and only for reference.
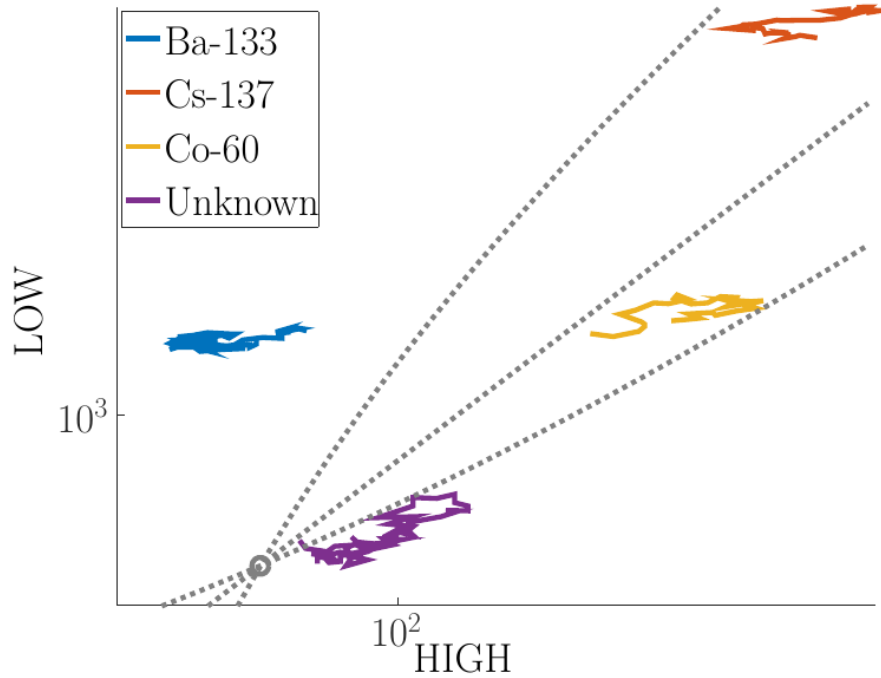
Figure 14. Moving mean graphs of the HIGH-LOW data shown in Fig. 13. All data is offset for a single background point (grey circle). Grey dashed lines are linear and only for reference.
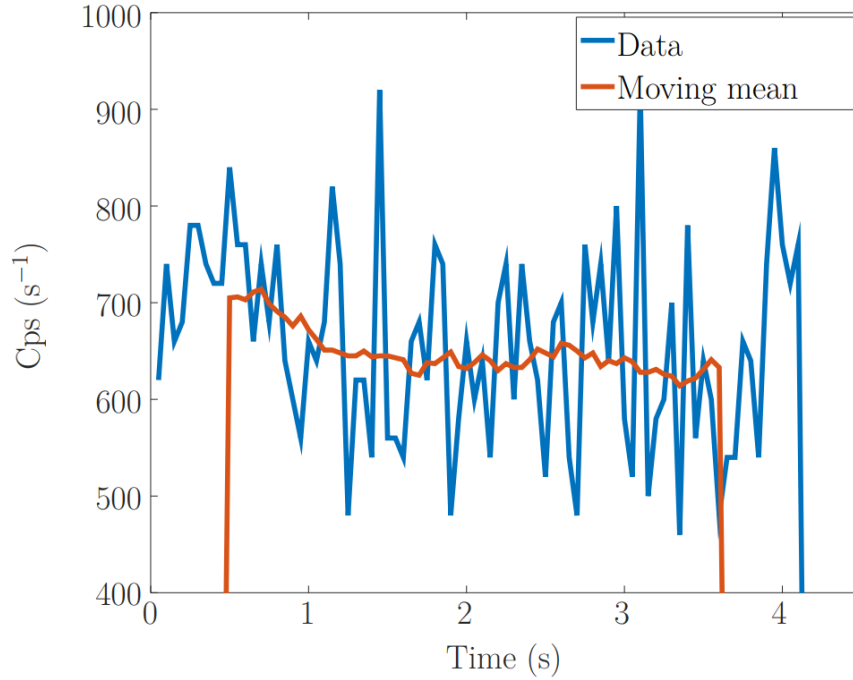
Figure 15. The LOW channel of a measurement of a moving vehicle.

4.4 Multichannel method

In order to make the source identification more accurate one can divide the channels further. With the third energy window one can try to separate a specific nuclide, e.g. ^{40}K, or to divide the LOW channel into two. In general, as one adds more channels, the individual ratios between the channels become more complex and unique to different sources. One prominent energy window would be to distinguish α-Be and fission neutron sources by probing gammas at up to 4 MeV [3] since most radiation monitors also have separate neutron detectors. While all neutron alarms should be investigated, a preliminary information for a possible fission source, such as 252-Cf, is valuable.

Because the number of possible values, sums and ratios increases rapidly with the number of energy windows it can be feasible to create new methods for identification. Increasing the number of energy windows will eventually lead to a spectrometric analysis. One tool for spectrometric nuclide identification is a fitting procedure which is an application of the numerical method presented in 5.3. Here, a specific function is fitted to the background subtracted spectrum resembling the Compton continuum of a photopeak. From there one can obtain the original photopeak energy and proceed to a regular nuclide identification process.

5   Characterization techniques

Three different techniques were applied to probe the PS's condition and for calibration purposes. In section 5.1 we scan through PS with a collimated source in search of defects or other structural non-uniformities. Section 5.2 presents a method to evaluate the attenuation length of the scintillation material that doesn't require any disassembling of the radiation monitor. Finally, in section 5.3 we make use of the Gaussian distributed energy components and create a numerical fitting method for energy and resolution calibrations which can be utilized to nuclide identification.

5.1   Defect probing

The uniformity of the scintillation material is checked to detect any major defects such as cracks or localised dusky spots in the scintillation material. Defects of this nature all result in significant light yield loss in the scintillation material which in turn reduces the efficiency of the radiation detector. The defects can be induced both in the manufacturing process and due to ageing effects.

One non-destructive method is to scan the whole scintillator over a matrix. This setup is also field-operable as it doesn't require disassembling of the radiation monitor as long as the gamma rays can sufficiently penetrate the casing of the monitor.

5.1.1   Probing: Measurement setup

The signal from the PS is led through an inverter to MCA similarly as in Section 4.1.2. MCA is used to get spectra from every measurement only in case we need additional information, but most of the analysis can be done by simple counters. The radiation sources used are ^{137}Cs and ^{241}Am where the former is used for internal and latter for surface probing. The measurement time was 120 seconds per location.

We can calculate the absorption probability P according to the equation

$$P = 1 - e^{-(\mu/\rho)x} \tag{6}$$

where μ/ρ is the mass attenuation coefficient, $x = d \cdot \rho$ is the mass thickness, ρ the density and d the depth. Using the data from [10] shown in Fig. 2 in Section 2.1, the mass attenuation coefficient μ/ρ is 0.1893 cm^2/g at 59 keV and 0.084 cm^2/g at 662 keV. Assuming the density of 1.023 g/cm^3 from Table 1 at Section 2.1 we can compute that 50% of the gammas with energies 59 keV and 662 keV have undergone
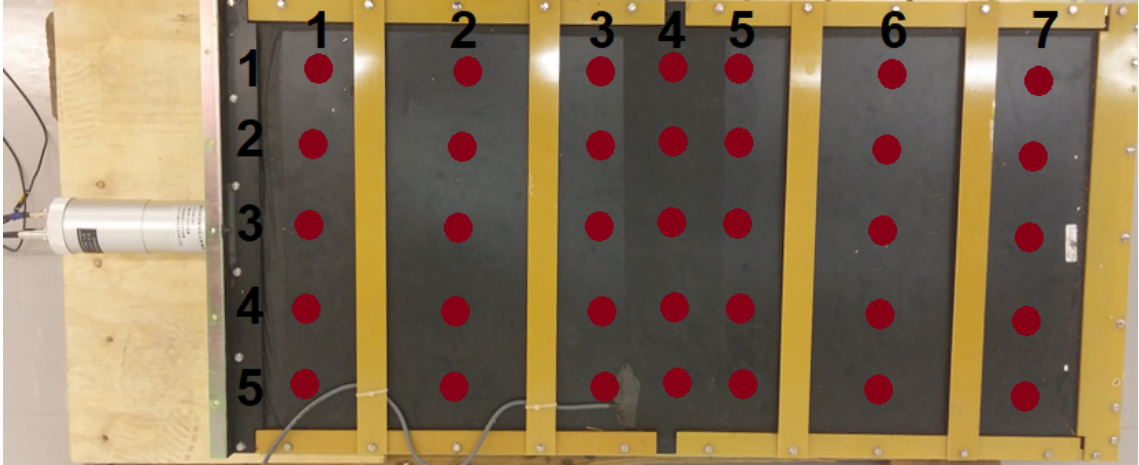
Figure 16. The measurement locations and their labels used in the defect probing measurements.

absorption in depths 3.58 cm and 8.06 cm, respectively. For comparison, the PS case thickness altogether is 11 cm including a probable lead shield on the back side.

The radiation sources were collimated using a lead cylinder with roughly 1.5 cm thick wall and a 2 cm diameter hole at the bottom. The collimated source was measured in different locations over the PS. By measuring the cps in each location we can form a contour map which reveals the information from the light propagation inside the scintillation material. Due to a constant background, there is no need for background subtractions to normalize separate measurements[6].

The probing was done in a 5-by-7 matrix as shown in Fig. 16.

5.1.2 Probing: Results

From the ^{241}Am and ^{137}Cs measurements we can create contour maps showing the total count rates. These are shown in Fig. 17 and 18, respectively. From the figures one can easily conclude that the count rate decreases as we go further from the PP, which is expectable as light travels further through medium. In both cases the corners at the PP's end are significantly dimmer than in the middle which shows the lack of light guide between the scintillation material and PMT. In the case of ^{241}Am, there is a clear decrease in count rates at the edge in the middle of the PS (location 5,4) which is exactly the location of an assumed thermometer. The whole middle part has lower count rates in general implying additional material between the source and PS. Note that these effects are not visible with ^{137}Cs measurements as its gammas penetrate the surface relatively easily. On the other hand, the effect of being closer to the edges are far more visible with ^{137}Cs.

---

[6]Our signal is also well distinguishable from the background as discussed at the results section.

40
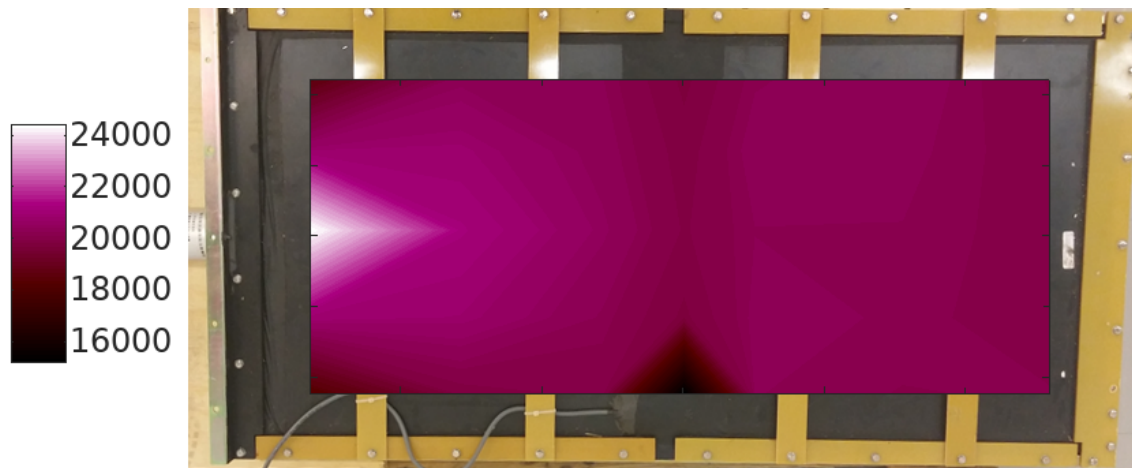
Figure 17. Results from the probing measurement using ^{241}Am source
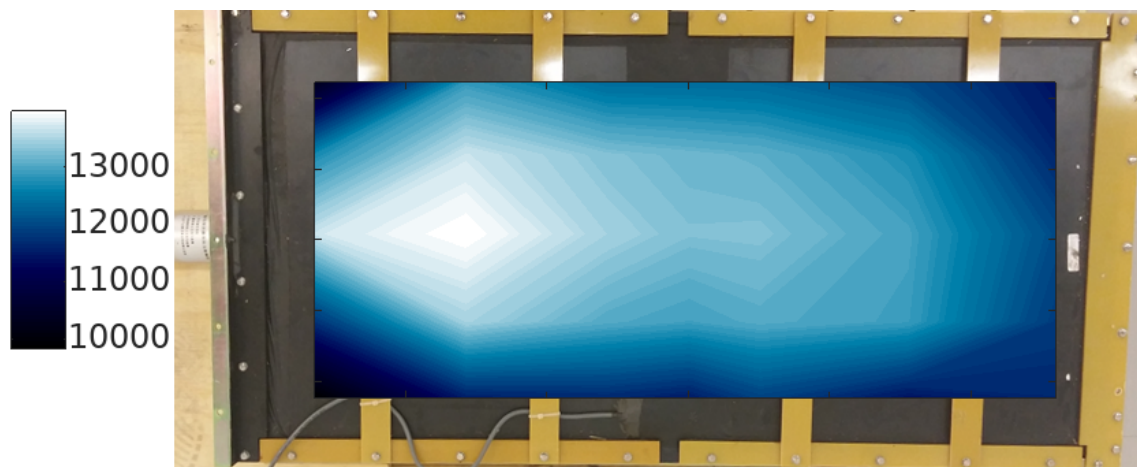
Figure 18. Results from the probing measurement using ^{137}Cs source
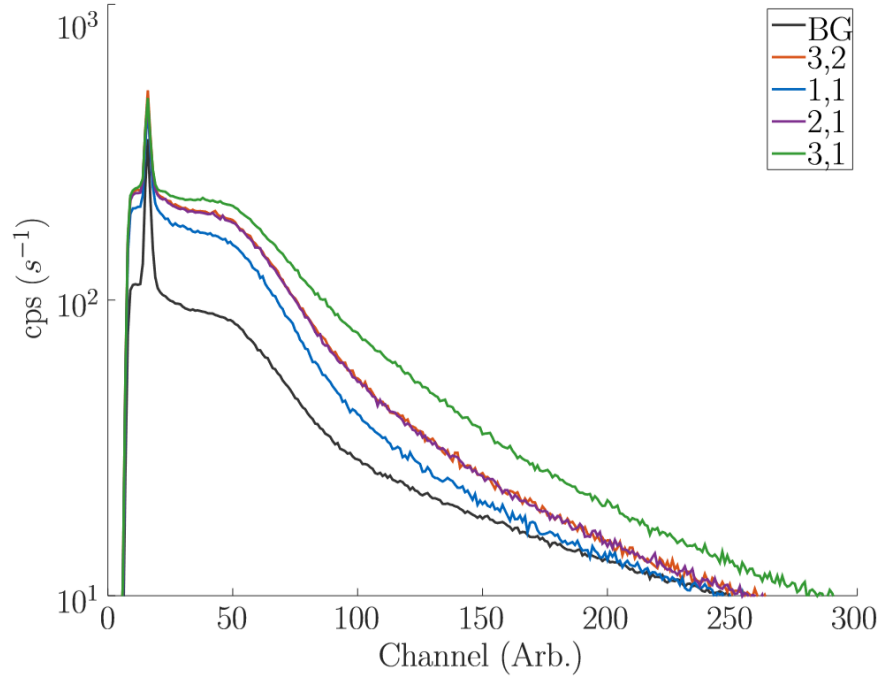
Figure 19. Part of the energy spectra measured near PMT using collimated ^{241}Am source. Labels are coordinates as in Fig. 16.
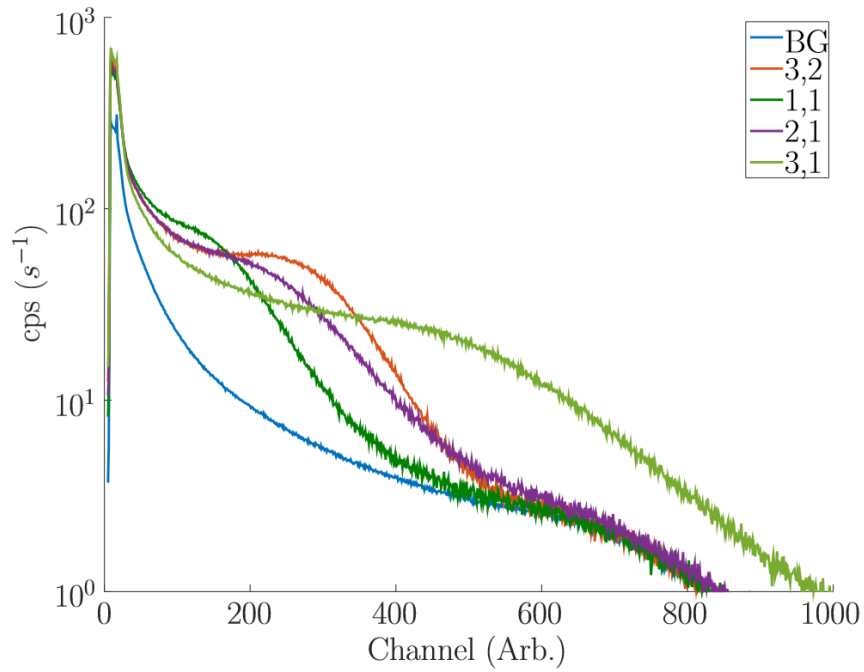
Figure 20. Part of the energy spectra measured near PMT using collimated ^{137}Cs source. Labels are coordinates as in Fig. 16.

^{137}Cs measurement shows unexpected behaviour where the count rate drops as we get closer to the PMT on the central line. From the measurement spectra shown in Fig. 19 and 20 it is clear that the ^{137}Cs spectra becomes anomalous near the PMT. Possible cause is that a significant portion of the gammas can reach the PMT bypassing the scintillation process. Thus data from these locations should be taken cautiously. Similar, but less significant, effect is visible also in case of ^{241}Am.

5.2   Attenuation length using coincidence method

As the plastic ages it becomes foggy due to small defects and other damage caused by different ageing processes. This reduces the attenuation length especially for the scintillation photons, the length of which light can travel through the medium until its intensity reduces to one e'th. When ageing less photons reach the PMT created by the same initial gamma energy, which in spectrum analysis can be seen as a spectrum scaling towards zero. While this can be compensated by amplifiers, the major problem arises from the unideal electronics. Artefacts at the low voltage region due to e.g. bad grounding are always relative to the scintillation signals and need to be cut off for proper spectrum or energy window analyses. Ultimately, as the scintillation material ages and the signal voltages become lower, low energy sources such as ^{241}Am cannot be feasibly detected.

The countermeasure is to simply replace the plastics to new ones. In case of multiple radiation detectors the cost of replacing all the plastics might cumulate to a significant expense. Thus it is convenient to monitor plastics' condition and replace them only when needed. Individual plastics also age at a different pace, so replacing only the unusable ones also evens out the expenses on longer period.

A way to monitor plastics' condition is to measure their attenuation lengths over their lifespan. An affordable and field-deployable method is presented here and also shown to work on field without disassembling the radiation monitor at all. Another characteristic to probe is the (relative) energy resolution R, which is defined as the ratio of the full-width-half-maximum (FWHM) and the mean μ of measured spectrum for single-energy scattering events.

The goal of this experiment is to probe the duskiness of the scintillation material. Different environmental and radiation deduced ageing effects from have been shown to create defects in the surface and within the scintillation material. Because the PS used in this thesis is an old one these effects are assumed to be present throughout the scintillation material. A photograph taken from the PMT connection region of a similar scintillator that had undergone same environmental effects is shown in Fig. 21 where white defected spots are clearly visible. The defect points are not only on the surface but also deep within the scintillation material. Similar visible defects are also reported in Ref. [14].

Figure 21. A photograph of a similar PS showing visible defects caused by ageing effects. The defects are also within the scintillation material and not only at the surface.

5.2.1 Attenuation length: Measurement setup

The setup's goal is to examine the propagation of scintillation photons along the PS. For a systematic analysis a constant intensity light source with corresponding wavelength is required. The solution in this thesis is to investigate a single Compton scattering energy. Because the number of scintillation photons created per energy deposited is near to constant, interactions with a fixed energy act as a flickering photon source within the scintillation material. For other scintillator systems, examining the photopeaks or simply using a light emitting diode (LED) could be more convenient. Neither of these methods are possible because the PS only interacts with the gammas at our energy range of interest via Compton scattering (as shown in Fig. 1 of Section 2.1), and installing the LED requires disassembling of the PS casing. In contrast with using an LED, the wavelength of propagating photons are also naturally at the region of interest when created via scintillation process.

The Compton scattering events chosen for the measurements are the full backscattering events where the initial gamma does a 180° scattering from the plastic. In order to filter out other scintillation events, a secondary scintillator with appropriate energy resolution is required to detect the backscattered gammas. In our measurement we used two different cylindrical lanthanum bromide ($LaBr_3$) crystals (both Saint-Gobain BrilLanCe 380) with sizes, 1.5"×1.5" and 3"×3" as their length and diameter, respectively. The $LaBr_3$ were mounted onto a PMT base (Ortec ScintiPack, model 296).

Four sets of measurements were done. First the PS used throughout this thesis was evaluated in laboratory conditions with both 1.5" and 3" $LaBr_3$s. Then, two similar

operative PSs were evaluated using the 1.5" LaBr$_3$. In the measurement setup, the secondary scintillator and the source are positioned as shown in Fig. 22. The on-field measurement setup is shown in Fig. 23. The distance from the source to PS was roughly 5 cm and the distance from LaBr$_3$ to the source was roughly 3 cm. These distances were kept short to minimize the backscattering events that could occur farther along the PS.

The LaBr$_3$ is now set to detect only the backscattered gammas which have a specific energy. The events in PS simultaneous with the ones detected in LaBr$_3$ then correspond to the backscattering event itself. This is called as a coincidence method. In our setup we led the signal from PS through an inverter to an analogue delay module (Ortec 427A) and fed to the MCA's input. In the 1.5" lab measurement set an amplifier (Canberra 2111) with a 10x gain was used in PS signal line to enhance the channel resolution in MCA. In calculations the channels were scaled back by dividing the channels by a factor of 10 for comparison purposes. The signal from LaBr$_3$ is led through an amplifier (Ortec 572A), single channel analyser (SCA, Ortec 550), gate and delay generator (G&D, Ortec 416A) and finally fed to MCA's gate input. The SCA module gives out a logical pulse with a width of 500 ns if and only if the amplitude of the input signal is within a set amplitude window. This window will be set to match the mentioned backscattering energy. The gate and delay generator is used to adjust the width of this pulse so that the signal from PS is within the logic pulse. The delay module in PS signal line is to move the signal within the said logic pulse. The final signals from an event is shown in Fig. 24.

For field measurements all the modules were mounted on a nuclear instrumentation module (NIM) rack with an in-built power supply (Ortech Minibin, 4006). The measurement equipment is shown in Fig. 25.

Both the delay module and amplifier in PS signal line scaled the amplitudes linearly and didn't change the pulse width significantly along the whole amplitude range of interest (not shown here). This is mandatory since the attenuation length is dependent on the relative amplitudes between different measurements.

The requirement for the radiation source is an easily distinguishable backscattering peak. In our measurements we used ^{137}Cs which emits only 661.657 keV gammas which according to Eq. (1) has a backscattering peak at

$$E^* = \frac{661.657 \text{ keV}}{1 + \frac{661.657 \text{ keV}}{510.999 \text{ keV}}(1 - \cos 180°)}$$
$$= 184.322\ldots \approx 184 \text{ keV}.$$

This is well distinguishable from the backscattering peaks of ^{40}K and ^{208}Tl which are at around 250 keV. Conveniently, the energy is also high enough to penetrate the radiation monitor casings in our field demonstration.

Coincidence requirement with backscattering peak in LaBr$_3$ means that the energy
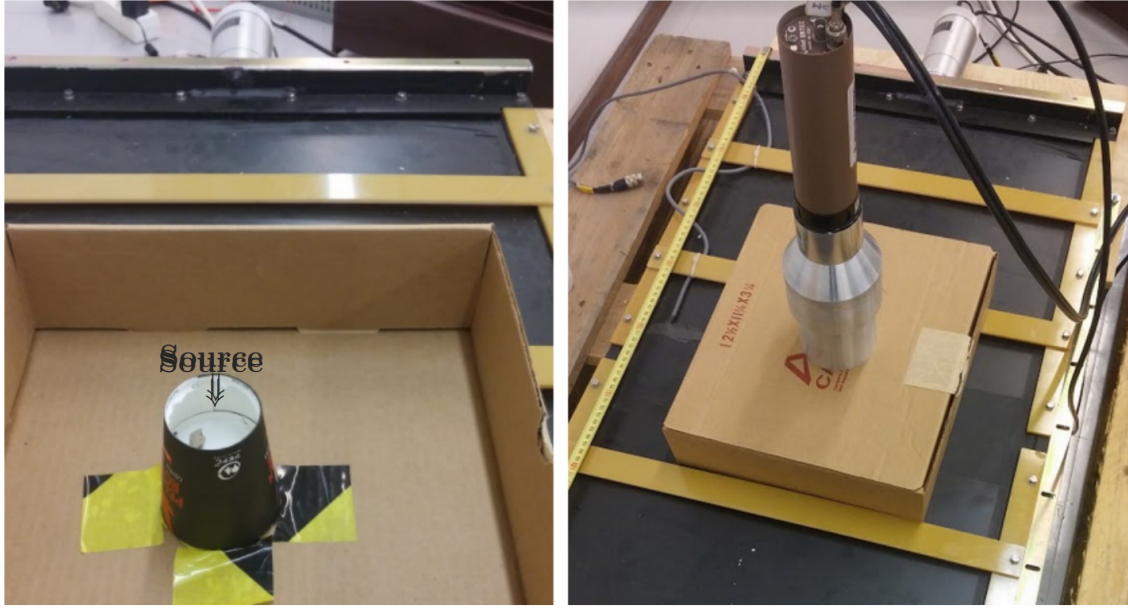
Figure 22. The scintillator setup for coincidence measurements. The radiation source is placed in the source holder (left image) which is placed between PS and the secondary scintillator (right image). The secondary scintillator in the right picture is the 3" LaBr$_3$.

deposited to PS is

$$661.657 \text{ keV} - 184.322 \text{ keV} = 477.335 \text{ keV}$$
$$\approx 477 \text{ keV.}$$

The gate region is first defined using self-gating technique, where the input to delay module is replaced with the signal divided from the LaBr$_3$'s amplifier module. Now, whenever the gate opens, the signal is accepted to the MCA. This allows an easy adjustment of the SCA window. In Fig. 26 is shown the spectra measured with and without self-gating.

With this setup, spectra were gathered from along the center line of PS as shown in Fig. 27. The line needs to go along the center line to have equivalent edge interactions.

Figure 23. The measurement setup for attenuation length measurements on the field. The PS is inside the blue metal casing upright and the hanging 1.5" LaBr$_3$ is facing the monitoring side.
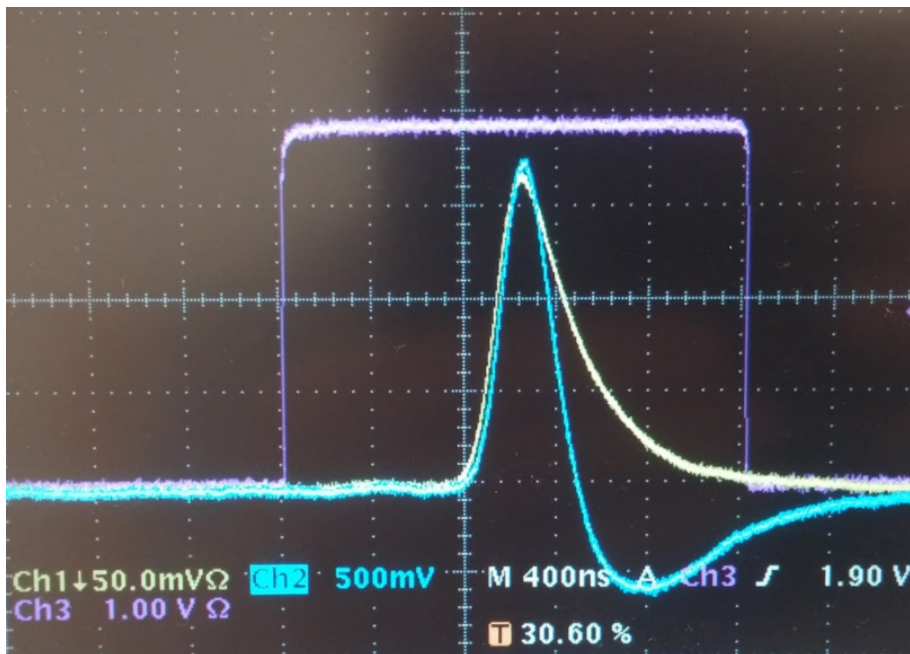
Figure 24. The delayed signals from (Yellow) PS before the amplifier, (Teal) PS after the amplifier and (Purple) the "gate signal" at the end of LaBr$_3$ signal line.
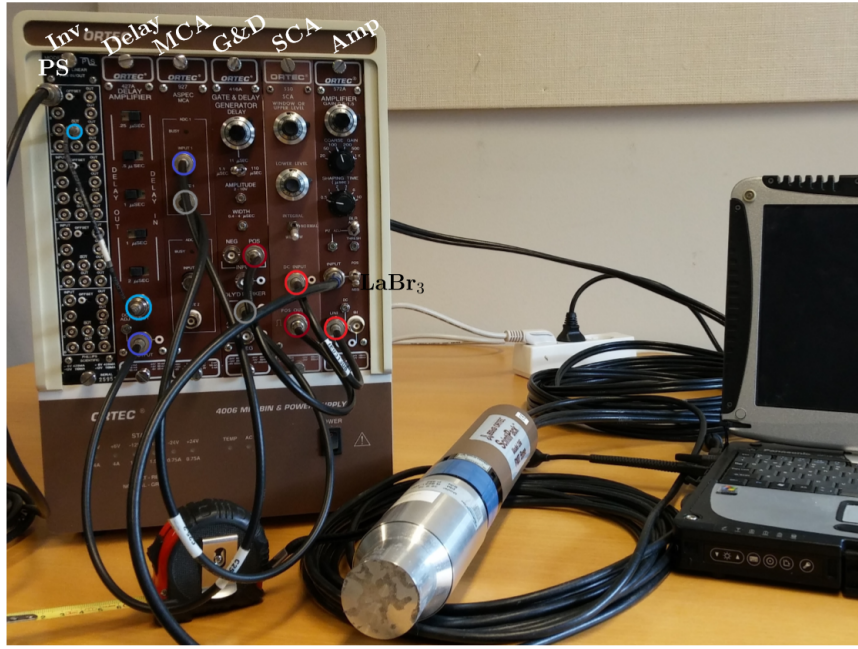
Figure 25. The measurement equipment and module wiring used for the coincidence measurements. The LaBr$_3$ scintillator in the picture is the 1.5" BrilLanCe 380.
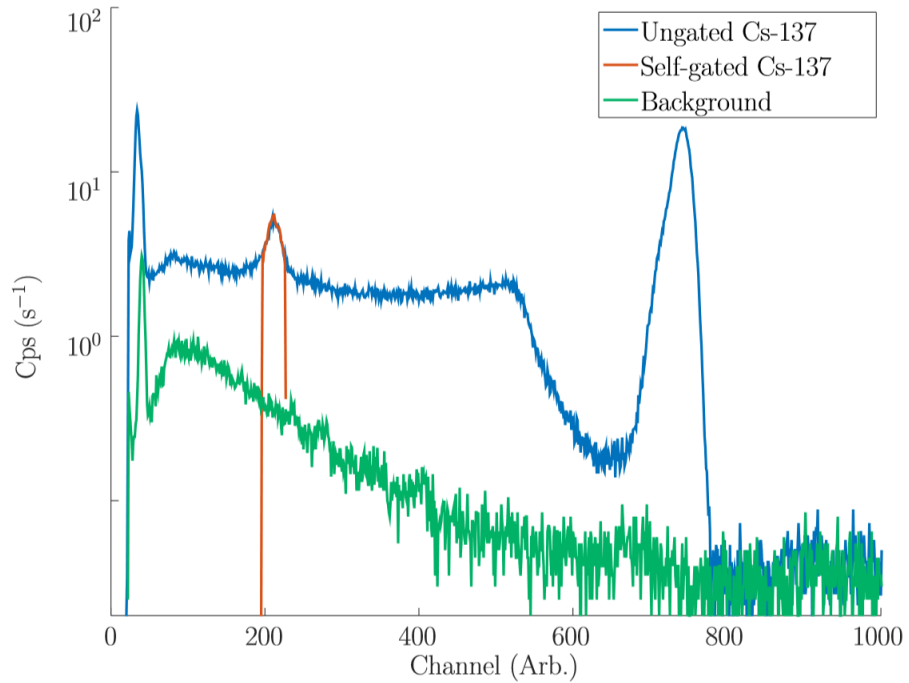
Figure 26. Spectra from 1.5" LaBr$_3$ with and without self-gating ^{137}Cs source, as well as the background spectrum for reference. The red curve shows the region to be used as gate.
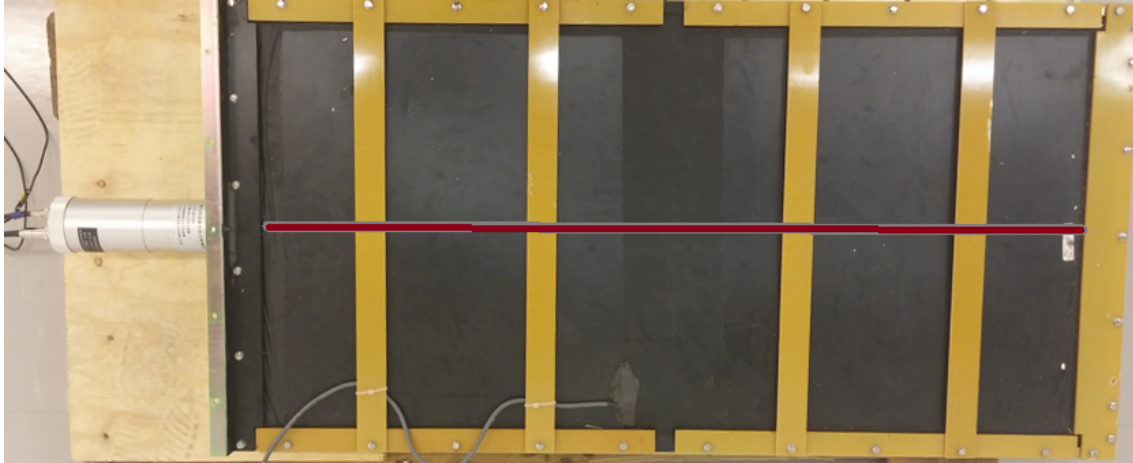
Figure 27. The attenuation length spectra are gathered along the red line shown.

5.2.2 Attenuation length: Single spectrum analysis

We first try to understand the components of the gated spectra by analysing a gated PS spectrum gathered from a single location using a ^{137}Cs source and the 1.5" LaBr$_3$.

The approach is to use four different gates shown in Fig. 28. Of these four gates two are at the backscattering peak with different widths and ones on both sides from the backscattering peaks. We can predict that the width of the gate at the backscattering peak should only affect the intensity of the gathered spectra and not the location of its peak. The gate to the left probes events where the 662 keV gamma has deposited more energy than a single 180° backscattering but not yet all of its energy, or put shortly, multiple Compton scatterings. The gate to the right has lower limit at 233 keV [7] corresponding to a Compton scattering at angle 115°. For a gamma to scatter from PS to LaBr$_3$ at this shallow angle is practically impossible in this geometry. Therefore this gate probes mainly background and random coincidences where two gammas are emitted within an event time window. The right-shifted gate therefore produces the best approximation for the background spectrum.

The PS's spectra resulted from the gates of Fig. 28 are shown in Fig. 29. To the "normal", "slim" and "left"-gated spectra we created a 8th order polynomial fit to find quickly the location and height of the peak. The left-shifted gate still has similar trend as the normal and slim gate's, but the right-shifted gate with its smoothness does express the behaviour of the background the best as speculated earlier in this section. The width of the "normal" gate was roughly double of the "slim" one and when the slim-gated values are scaled by a factor of 2, its r^2-value between the normal-gated spectra is 0.9968. This supports the intuitive effect of the change in gate width.

---

[7]Energy calibration for LaBr$_3$ obtained from Section 5.3.4.
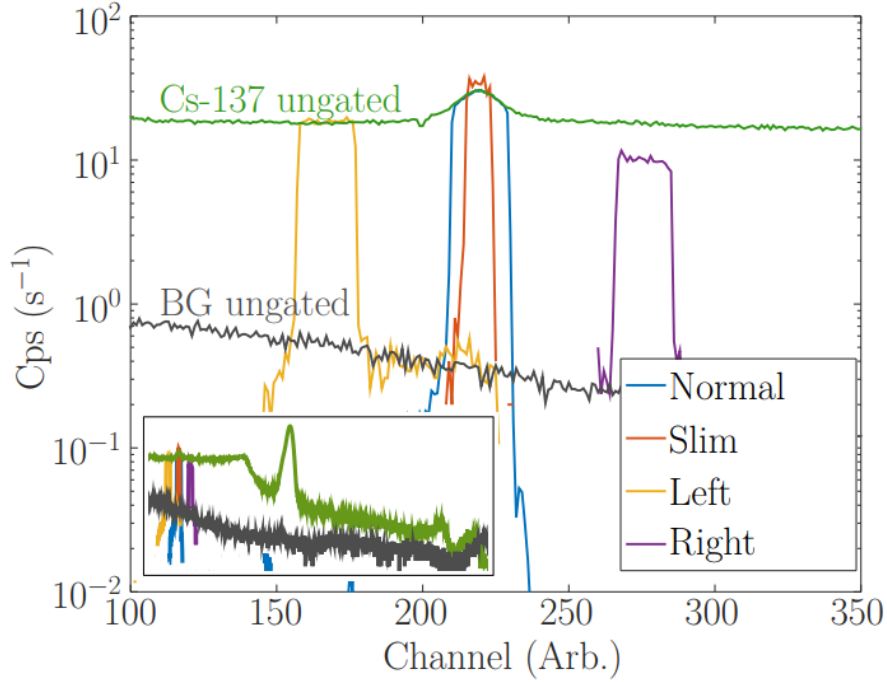
Figure 28. LaBr$_3$ spectra of the different gate locations measured using the self-gating technique. Inset: broader x-axis from channel 1 to 1800.

The background without a present source was also measured using the normal, left and right gates. The count rates were all 2 magnitudes lower than the right-gated ^{137}Cs spectrum (not shown) which renders the background radiation's contribution to the gated ^{137}Cs spectra insignificant. The right-gated ^{137}Cs spectrum therefore probes the random coincidences.

While the right-gated spectra is half the magnitude weaker than our signal peak, it does create a skew to the spectrum, which in turn might affect to the location of our peak. Using the right-gated spectrum as the background, we subtract it from the normally gated one. As shown in Fig. 30 the resulting spectrum has a smooth Gaussian shape, although slightly positively skewed, and represents one candidate of a background subtracted spectrum.

Gaussian curves were fitted to the normally gated spectrum before and after subtracting the right-gated spectrum. The fitting region of interest is shown with the plot and the corresponding r^2 values are 0.997 and 0.993 for normally gated and subtracted spectra, respectively. The mean location μ increases for one whole channel after subtracting the right-gated spectrum while the fitting uncertainties became of one magnitude lower. With this knowledge we can give the mean location μ an error estimate of 3% which is 1.6 channels for the normally gated spectra. Because the normally-gated spectrum has slightly higher FWHM we can set it as an upper limit. The uncertainty of normally gated FWHM can also be taken as 1%. This gives us a feasible approximation of the worst-case-scenario for the resolution.
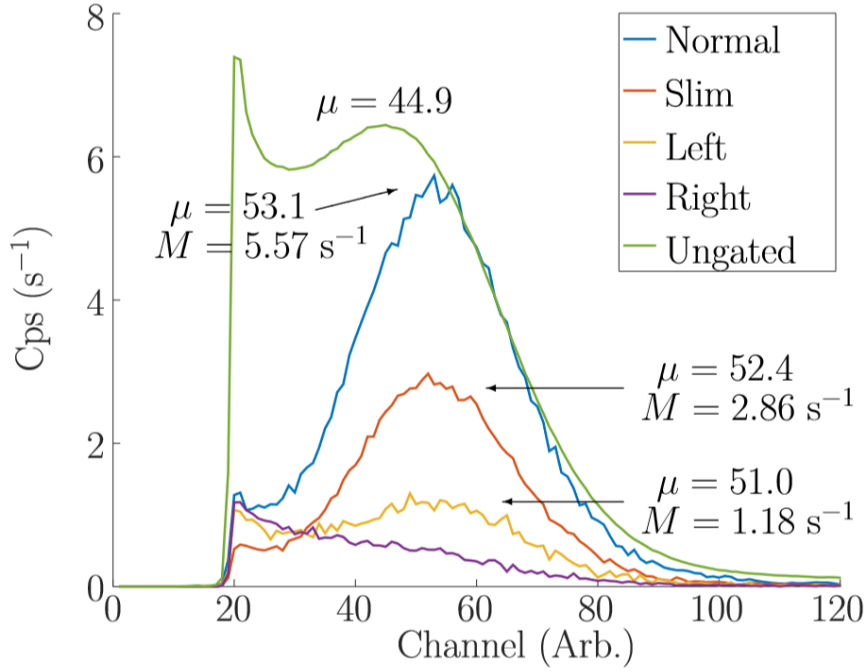
Figure 29. PS spectra acquired using the gates shown in Fig. 28. The ungated spectrum is scaled by a factor of 7.5e-3. μ and M corresponds to the peak's location (channel) and height (cps), respectively.

One option for future spectrum analysis is to use the linear fits for the random coincidence spectrum. This is left undone in this thesis as the development of the right-gated spectra by distance from PMT or source intensity wasn't investigated further.
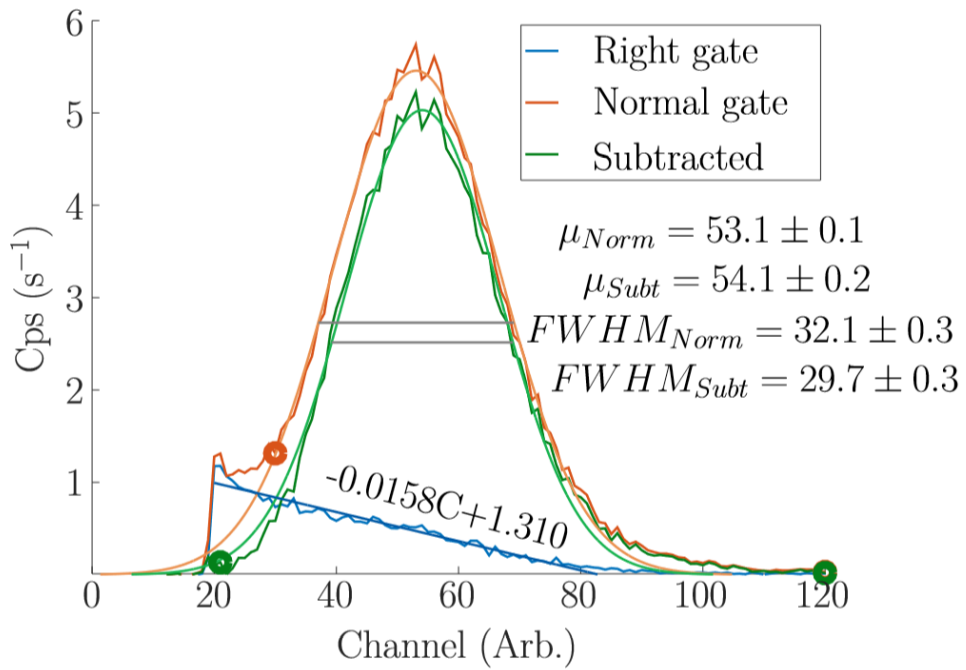
Figure 30. PS spectra gated at and right from the backscattering peak, and their difference. Gaussian fits for the normally gated and subtracted spectra and linear fit for the right-shifted gated spectra with their parameters are also shown. Region of interest (ROI) for the fits are marked with thick circles.

5.2.3 Attenuation length: Results and discussion

The term distance is used here to describe the relative distances from the PMT. Since the scintillator casing was not opened, position of the PMT is estimated to be at 5 ± 2 cm. The location of the actual PMT interface does not affect the attenuation length, but rather the evaluation of absolute light flux created by one Compton scattering event which is not of interest here.

The error for the distance propagates mainly from the reading inaccuracy of the source. The diameter of the source holder where the source is able to move around is roughly 2 cm and the reading uncertainty for the source holder's location can be approximated as 1 cm, giving the distances an uncertainty of $\sqrt{5}$ cm.

To the gated spectra we create a 8th degree polynomial fit to find its maximum's location, μ, as well as the full width half maximum, FWHM. This process is done to all of the measured spectra. The spectra from all four measurement sets are shown in Fig. 42, 43, 44 and 45, and the extracted μ's and FWHMs in Tab. 4, of Appendix B.

We proceed by assuming the 3% uncertainty to μ values and the $\sqrt{500}$ mm uncertainty to the distances. An exponential fit is done to μ's as a function of distance for all four datasets (method discussed in Appendix A). The final fits with datasets are shown in Fig. 31. As the distance gets longer the μ's decrease indicating the dampening of scintillation photon yield, as expected.

From the fits we can finally extract the attenuation length λ, which is shown in Tab. 2 along with other exponential fit parameters. The obtained attenuation lengths are drastically shorter than the ones given for fresh commercial PSs' in Tab. 1. This is a clear indication of ageing and implies the need of renewing the scintillation material.

The behaviour of FWHM tells us how the resolution changes along the PS. The absolute values of FWHM are rarely used as a resolution measure, but rather the relative resolution R, where the FWHM is divided by corresponding energy. Our energy is constant as all our events are from 477 keV Compton scatterings, so in perspective the location of μ can give us more insight of the behaviour within the scintillation material. The absolute FWHMs are shown in Fig. 32 and the channel-relative resolutions in Fig. 33. Given the uncertainties, the relative resolutions stay the same along the whole PS, where the laboratory PS has a resolution of roughly 66% and the Field 1 and 2 PSs have relative resolutions of roughly 66% and 90%, respectively.

The coincidence method has been used in literature for energy calibration [13] by using different single-energy radiation sources. The fraction $(CE - CM)/CM$, where CE is the location of Compton edge and CM is the location of Compton maximum, is reported to be roughly linearly growing function of initial gamma's energy, and differs among scintillator systems. In this paper, the fraction was evaluated to be 5.5% for BC408 type plastic scintillator at 662 keV. As we were lacking multiple

single-energy gamma sources, we also lack a proper energy calibration. Reading our values from the Fig. 29, $CE = 53.1$ and $CM = 44.9$ in channels which results in the fraction 18.3%. We will revisit this matter in Section 5.3.4.

The attenuation length has also been measured in literature. A. Artikov et al [1, and references therein] have measured periodically the attenuation lengths for multiple polystyrene scintillators using an LED since 2002. Their results show a decreasing trend in both the attenuation length λ as well as the yield (denoted as A in Table 4) by age. During seven years as components of a muon detector, the attenuation lengths have decreased roughly 100 cm from the initial 400 cm and 500 cm for their two separate scintillators. Their results motivate PS users to keep track of the attenuation length as it gives an estimate how each individual PS ages. Setting a lower limit for the coefficients one can foresee when a specific PS should be replaced or undergo maintenance. Their main methodological difference when compared to our case is using an LED as a photon source instead of utilizing a secondary scintillator. The latter allows the evaluation to be done without unwrapping the scintillator in case a calibration LED is not installed pre-emptively. Another difference is that unlike in Ref. [1] our scintillator is not painted black at the far end which allows scintillation photons to reflect from it. This results in an exponential behaviour that does not need a levelling constant (denoted as B in our fit function, see Table 2).

The coincidence method used here has its limitations as we probe with the secondary scintillator only the backscattering events. K. Roemer et al [11] used similar setup with so called multi-parameter data acquisition system, labelling all events in both scintillators with a time signature. This allows one to gather spectra from both scintillators independently without gating and synchronize the acquired data according to the time signatures, unveiling the coincidence events. This method is not restricted by the backscattering peak and allows one to use higher gamma energy sources, such as ^{60}Co or ^{40}K. Our coincidence spectra would correspond to one cross section taken at a fixed energy. While they were focusing mainly on the resolution calibrations, the energy calibration would be easily achievable as well. The attenuation length was not evaluated in this publication, but it would consist of measuring these spectra along the PS and forming energy calibrations as a function of distance.

Table 2. The parameters of the fits shown in Fig. 31

$$\mu = A \cdot e^{-d/\lambda} + B$$

Set	PS	LaBr$_3$	A (Arb.)	λ (cm)	B (Arb.)
Lab 1.5"	Lab	1.5"	30 ± 3	17 ± 1	38.7 ± 0.2
Lab 3"	Lab	3"	26 ± 3	20 ± 2	49.7 ± 0.2
Field 1	Field 1	1.5"	20 ± 10	15 ± 4	41.1 ± 0.3
Field 2	Field 2	1.5"	9 ± 3	50 ± 50	51 ± 4
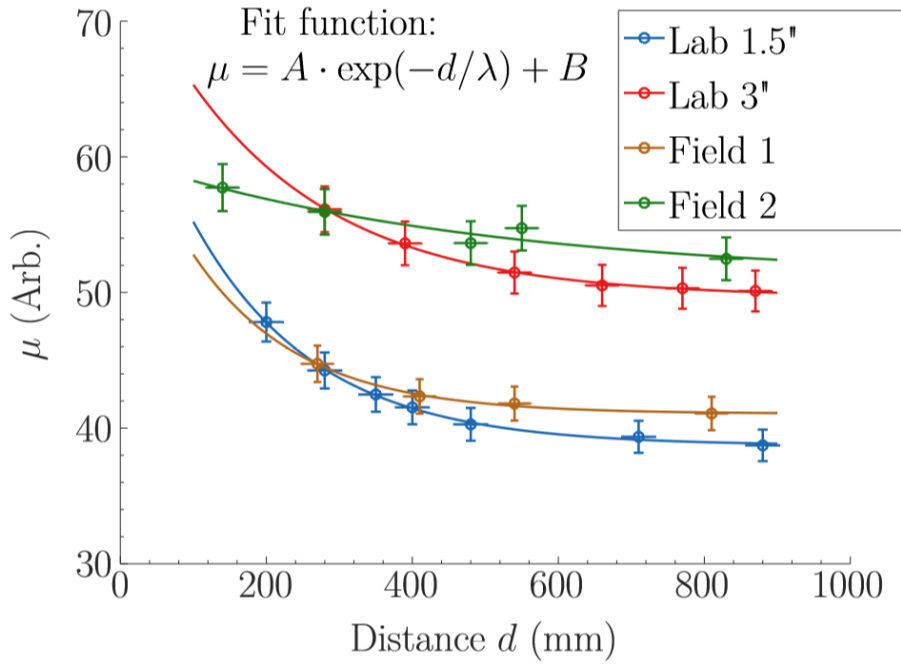
Figure 31. The means μ gathered from all measurement sets with exponential fits.
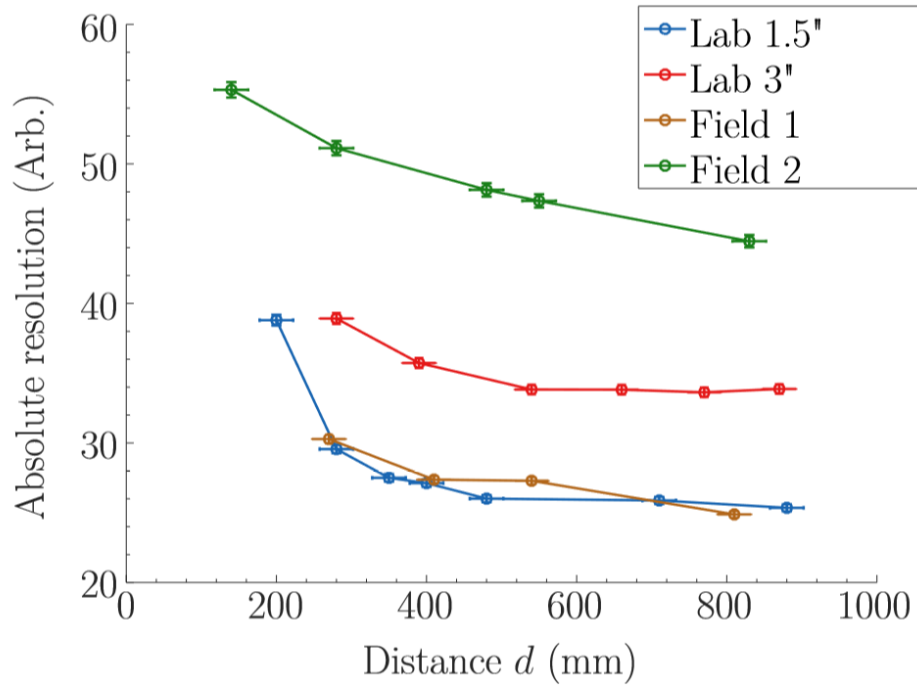
Figure 32. The FWHM's gathered from all measurement sets.
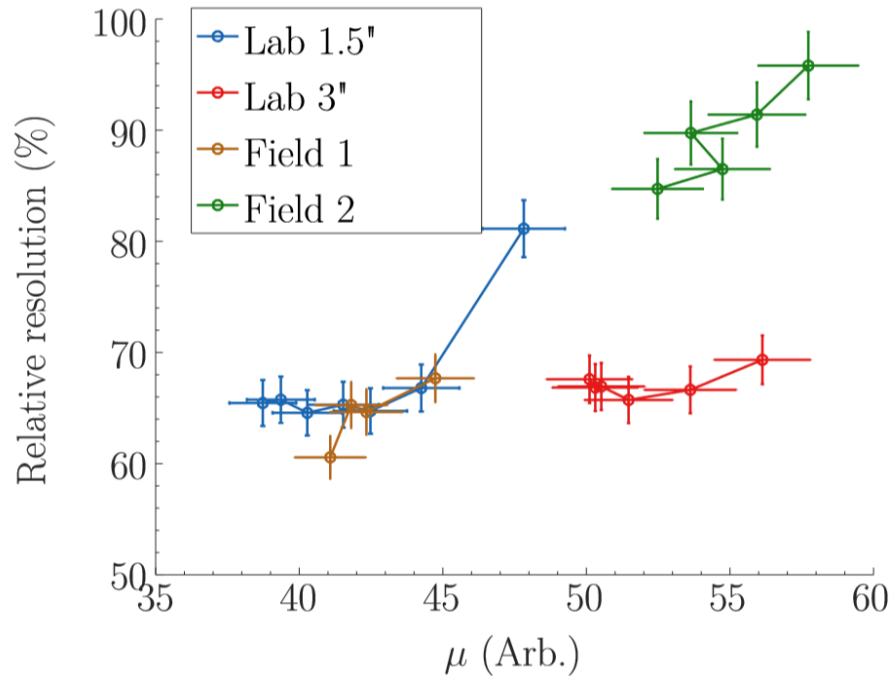
Figure 33. The relative resolutions gathered from all measurement sets.

5.3 Gaussian convolution: Numerical calibrations (GC)

This numerical method is used to determine the energy and resolution calibrations for PS [7, 4]. By fitting a convolution function between Gaussian distribution and Compton continuum (called GC-function herein) to a measured background subtracted spectrum, one can ideally simulate the resolution effect and extract the original location of the Compton edge.

5.3.1 GC: Theoretical background

As also seen in Section 5.2.2 the number of scintillation photons detected in the PMT in a single-energy event has a Gaussian distribution when observed with the MCA. Assuming a constant number of scintillation photons created by a single energy event, the distribution originates simply from the attenuation as the photons propagate within the plastic. Thus the Gaussian distribution should be present in every single energy of the Compton continuum with variance depending on the resolution at given energy.

Assume that the variance is a polynomial of the mean energy, i.e. $\sigma(E) = \sqrt{s_1 E + s_0}$, where s_1, s_0 are coefficients, as discussed in Ref. [6, p. 331]. A Compton continuum with each energy having a Gaussian distribution is simply a convolution of the two,

$$f(E) = k\left(\frac{d\sigma_{\mathrm{KN}}}{dE} * P\right)(E) = k\int_0^\infty \frac{d\sigma_{\mathrm{KN}}}{dE}(E^*)\frac{1}{\sqrt{2\pi\sigma(E^*)^2}}e^{-\frac{(E-E^*)^2}{2\sigma(E^*)^2}}\,dE^* \quad (7)$$

where $d\sigma_{\mathrm{KN}}/dE$ is the differential cross section presented in Section 2.2 Eq. (3) and k is a scaling coefficient. The function $f(E)$ in Eq. (7) is the written form of the GC-function.

Naturally, the resolution is implemented in GC-function as standard deviation $\sigma(E)$ via the relation $FWHM/E = 2\sqrt{2\ln 2}\sigma/E$.

Examples of graphs produced by Eq. (7) is shown in Fig. 34. The location of the Compton edge is further than the peak of GC-function, and the GC-function reaches further to the right the bigger the variance is, possibly over the photopeak location. The first observation was shortly visited in Section 5.2.3 and is discussed further after the results and compared with literature. The second observation is important when considering the low-energy gammas, especially the 59.5 keV gamma from ^{241}Am. Even if the photopeak location is below the cut-off region of the spectrum (under the static noise) the broad distribution can show a sign of the presence of the source. This is also discussed after the results.
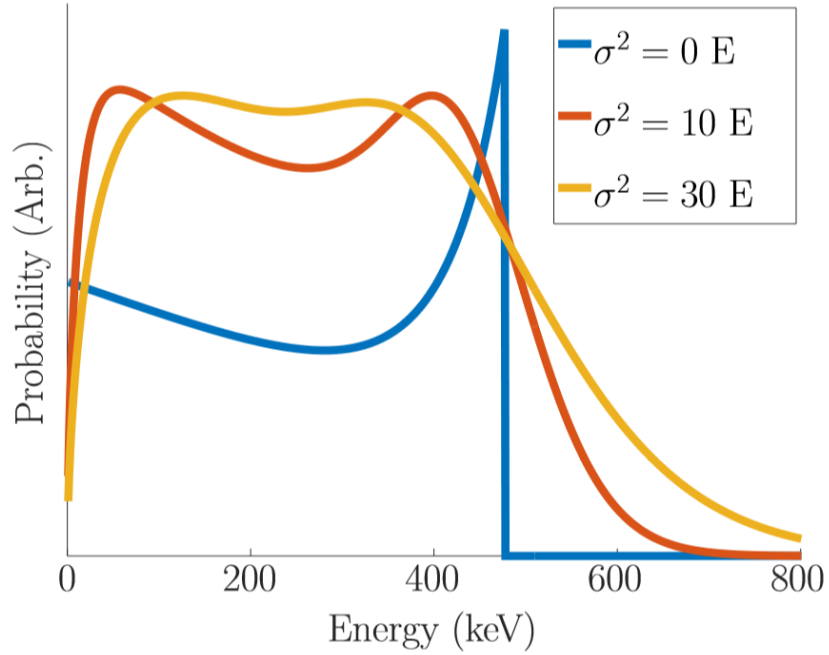
Figure 34. Examples of the GC-function with varying variances for a 662 keV gamma.

5.3.2 GC: Measurement setup

When creating the fits, one must also create an energy calibration for the collected spectra as we do not have a proper energy calibration for the PS yet. The energy calibrations are assumed to be quadratic polynomial at the region of the fit, i.e. $E(c) = a_2 c^2 + a_1 c + a_0$ where E is the corresponding energy in keV's, c is the channel and a_2, a_1, a_0 are coefficients.

To get initial energy and resolution calibrations three sources were used, namely ^{133}Ba, ^{137}Cs and ^{60}Co. These sources cover most of the energy region, with photopeaks at 356 keV, 662 keV and 1333 keV, respectively. With help of these calibrations the ^{208}Tl region from the background spectrum was fitted, which has a photopeak energy of 2614 keV. The resulted fit for ^{208}Tl was stripped from the background spectrum in order to fit the remaining ^{40}K (photopeak at 1460 keV) region. Here we assume that the background radiation is mainly originating from these two nuclides, namely ^{40}K and ^{208}Tl. The obtained ^{40}K fit was then compared to a background subtracted spectrum of ^{40}K source. The ^{40}K source was a bag of KO$_X$-rich fertilizer.

The initial three radiation sources were small point-like sources located in the middle of PS at approximately 20 cm distance from the face. The spectra were gathered by connecting the PMT to the MCA unit via the inverter.

5.3.3 GC: Fitting process

The Octave script used for the fitting process is shown in Appendeix C.

We have a total of six parameters for the fitting tool: three coefficients for the energy calibration (a_2, a_1, a_0), two for variance fitting (s_1, s_0), and an y-scaling parameter k as shown in Eq. 7. As seen from Fig. 34 the slope of the fit function near the Compton edge varies by variance. This slope can also be easily modified by changing the energy calibration. Furthermore, the variance is a function of energy which itself has parameters from the energy calibrations. This creates dependencies between our fitting parameters which can cause problems in individual fitting. To tackle this one could introduce conditions that the fit parameters or the fit function values must meet. Unfortunately, possibly due to the iterative fitting processes, this might distort the results as the process can consider the fit "accurate" when conditions are met at their very borders.

However, even when dependent, the energy and resolution calibrations scale differently as the energy calibration scales quadratically and resolution in an exponential manner. By realizing this we can fit three different spectra at the same time using the same parameters for all spectra, without conditioning. This allows greater precision than individual fitting processes enhancing the reliability of the results.

Another important factor is the region of interest for each fit. A good r^2 value for the fits at their corresponding ROI doesn't imply in this case a good calibration. The width of a ROI determines that fit's significance in the fitting process. Having a wider ROI increases the reliability of the fit for that specific spectrum but decreases the weight of other fits. Unnecessary widening of a short ROI decreases the weight of its interest region when already fully covered. Weighting the data according to its ROI is a possibility, but it was not explored further in this thesis. Ultimately, as long as the ROIs are at real regions of interest, wider ROI for a spectrum shall have more significance.

5.3.4 GC: Results and discussion

The fits created are shown in Fig. 35 and had a common r^2 value of 0.9948. In the figure, the light lines are the measured spectra, the dark lines the fits, the black dotted line is the non-convoluted Klein-Nishina used for the fit along with the photopeak, and the vertical light grey dotted lines show the ROIs used for each fit. The obtained fit parameters are shown in Table 3. All data is rescaled in y-direction for convenience.

The results are remarkably good regardless of the earlier speculation. The GC-function models the PS very well, and the low-end divergence of the fit and data in the case of ^{137}Cs and ^{60}Co could originate from the fact that our model completely ignores multiple Compton scatterings by one photon as well as the random coincidences from the surroundings in the laboratory. The linearity of the energy

calibration curve shown in Fig. 36 implies that even after many years the PS setup, especially PMT, can upkeep a consistent behaviour. Having a linear behaviour for the energy calibration also gives us a good insight of the future expectations of similar PSs.

With the obtained energy calibration, we revisit the discussion in Section 5.2.3, namely the fraction $r_C = (CE - CM)/CM$. With the energy calibration shown in Fig. 36 and the values for Compton maximum $CM = 44.9c$ and Compton edge $CE = 53.1c$, obtained from Fig. 29 of Section 5.2.3, we get a fraction $r_C \approx 19.1\%$. The energy of ^{137}Cs's CE is 477.3 keV. Using the parameters of the ^{137}Cs's fit function the location of CM is 381 keV resulting to a fraction of $r_C \approx 25.3\%$. By reading straight from the measurement data and using the obtained energy calibration, $CM = 372.4$ keV which results to a fraction of $r_C \approx 28.2\%$.

The resolution calibration curve obtained from the fitting process is shown in Fig. 37. In the figure the blue line is the obtained calibration and the red line is manually fitted Poisson model. The Poisson model assumes that the $FWHM$ is directly proportional to the square root of the given energy, or that $R = \frac{FWHM}{E} = K\sqrt{E}/E = K/\sqrt{E}$ where K is a constant. The obtained resolution calibration does show $FWHM$ to be notably non-linear, especially when considering the manual ^{208}Tl fit data point whose fit is shown in Fig. 38. The energy calibration was kept the same, only resolution calibration and y-scaling were manually adjusted. A non-linear behaviour of the PS system at higher energies is possible as we only fitted the energies below 1500 keV where the resolution and energy calibration behave remarkably linearly.

The resolution at 477 keV is roughly 56% which is 15% lower than the 66% obtained from the coincidence measurements in Section 5.2 Fig. 33. However, as discussed in Section 5.2.2, the coincidence spectra had a background contribution which when subtracted decreases the value of the resolution from 60% to 55% (Fig. 30). The result obtained with GC-method falls between these results increasing the credibility of this method.

As shown in Fig. 39 the obtained parameters do fit to background subtracted ^{40}K source well. For the concern of operative usage, energies above 1500 keV can all be categorized as NORM sources with the exception of neutron sources.

Shown in Fig. 40 we test our model by stripping the manual ^{208}Tl fit from the background and comparing it to background subtracted ^{40}K spectra, as our background radiation is expected to originate mainly from those two nuclei. While these do not overlap completely, there is a clear correlation between them.

Lastly, for the sake of reference, a GC-function fitted to ^{241}Am, ^{137}Cs and ^{60}Co spectra measured simultaneously with the 1.5" LaBr$_3$ used also in Section 5.2, along with the energy and resolution calibrations. A skewed normal distribution was used

to fit the photopeaks. The fit function $FIT(E)$ for the photopeaks is

$$FIT(E) = A \cdot \phi_S(E, \xi, \omega, \alpha) + B$$

$$\phi_S(E, \xi, \omega, \alpha) = \frac{2}{\omega}\phi\left(\frac{E-\xi}{\omega}\right)\Phi\left(\alpha\frac{E-\xi}{\omega}\right)$$

$$\phi(x) = \frac{1}{\sqrt{2\pi}}e^{-x^2/2} \tag{8}$$

$$\Phi(x) = \frac{1}{2}\left(1 + \operatorname{erf}\left(\frac{x}{\sqrt{2}}\right)\right)$$

where the fitting parameters are A, B for scaling and offsetting, ξ for location, ω for scale, and α for skewness or shape. For the energy and resolution calibration the mean μ and variance σ^2 values were extracted as

$$\mu = \xi + \omega\delta\sqrt{\frac{2}{\pi}} \quad \text{and}$$

$$\sigma = \omega^2\left(1 - \frac{2\delta^2}{\pi}\right), \text{ where} \tag{9}$$

$$\delta = \frac{\alpha}{\sqrt{1+\alpha^2}}.$$

The energy calibration was taken as quadratic and variance as linear, exactly like with the PS. The obtained energy and resolution calibrations from photopeak analysis were

$$E(c)\,[\text{keV}] = 1.2 \cdot 10^{-5}c^2 + 0.87c + 2.7$$

$$\sigma^2(E)\,[\text{keV}^2] = 0.36E - 83. \tag{10}$$

The calibrations were used straight for the GC-functions. The y-scaling for each calculated Compton continuum were done manually[8]. Separately measured background was used as a baseline. The created fits and the measured data are shown in Fig. 41. The red line shows the cumulative GC-function fits to each Compton continuum before applying the background. The yellow line shows the cumulative GC-functions fitted with the background along with the photopeak fits.

In Fig. 41 the factors that our GC-model doesn't take into account are clearly visible, namely the backscattering bump at energies 180–260 keV and the multiple Compton scatterings. The fit does follow the Compton continuum from the ^{60}Co gammas well, but worsens at the Compton continuum of ^{137}Cs. The most probable reason is backscattering from the surroundings. The backscattering spectra can be easily modelled by flipping the x-axis of GC-function, but as all scattering angles are not as probable due to the geometry of the environment, this correction was not further investigated. This could also explain the slope in the data between ^{137}Cs's photopeak and Compton edge.

---

[8]Same scaling factor was used for both ^{60}Co peaks.

Table 3. GC-function fit parameters obtained in Fig. 35. SE = standard error.

Energy calibration: $E = a_2 c^2 + a_1 c + a_0$			
Parameter	a_2	a_1	a_0
Value	2.92 e-3	8.01	-10.5
SE	1.14 e-3	0.23	9.5
Resolution calibration: $\sigma = \sqrt{s_1 E + s_0}$			
Parameter	s_1	s_0	
Value	32.7	-2740	
SE	1.0	440	

In literature, N. Kudomi [7] introduced the GC convolution function and established a correlation between the model and Monte Carlo simulated simulated data with high precision results. In 2016, C. Kim et al [5] formed fits using the same GC-function to evaluate the energy calibration and dose computation using a small polystyrene scintillator with notably higher resolution than ours. Their results indicated a linear energy calibration at sub-1000 keV energies as well.
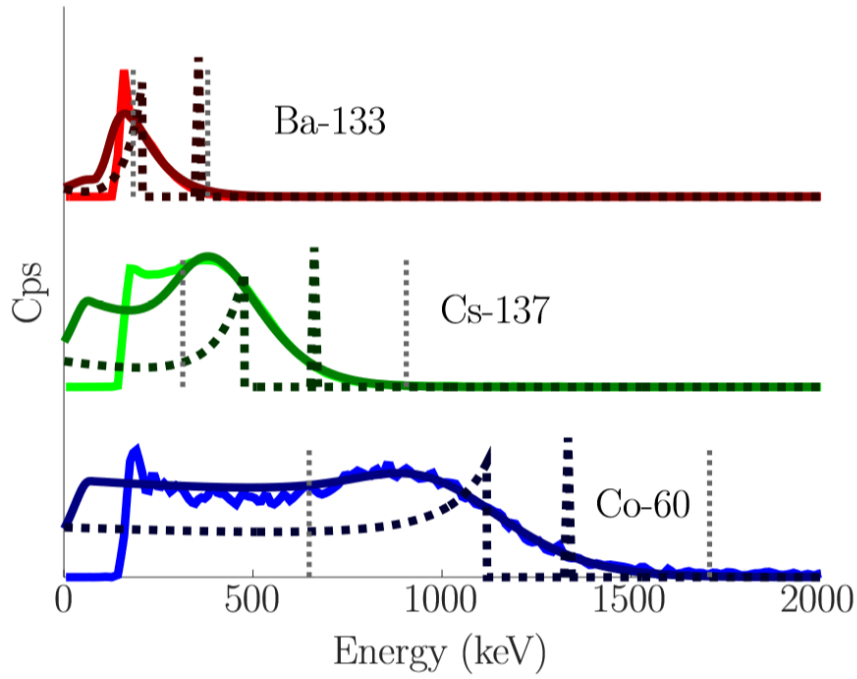
Figure 35. GC-function fitted to background-subtracted ^{133}Ba, ^{137}Cs and ^{60}Co spectra. Lighter lines: measurement data. Darker lines: the GC fit. Black dashed lines: unconvoluted Klein-Nishina. Grey vertical dashed lines: ROI limits.
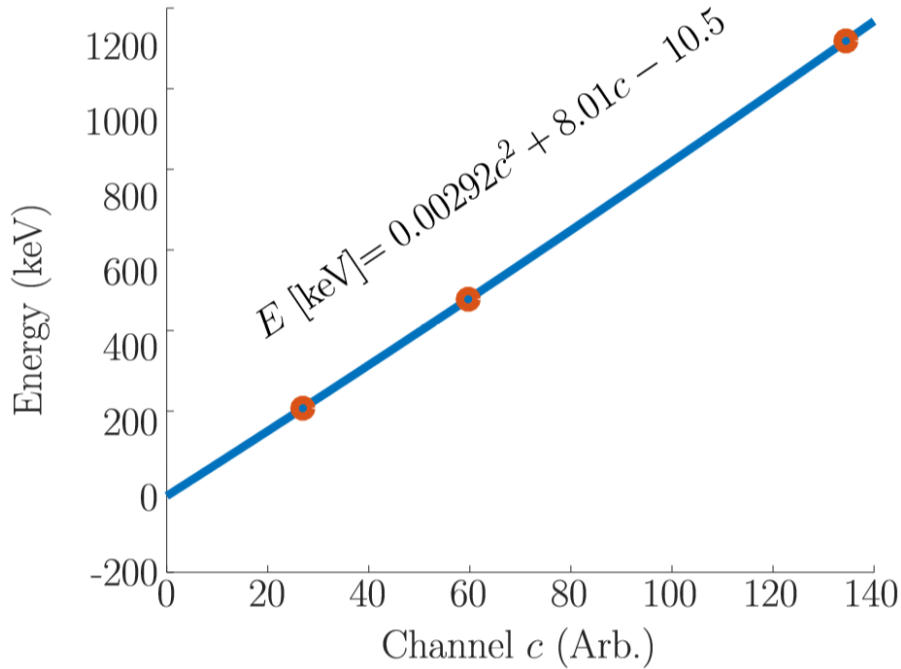
Figure 36. Energy calibration curve obtained from the fits shown in Fig. 35. The red circles show the locations of the Compton edges of the fits.
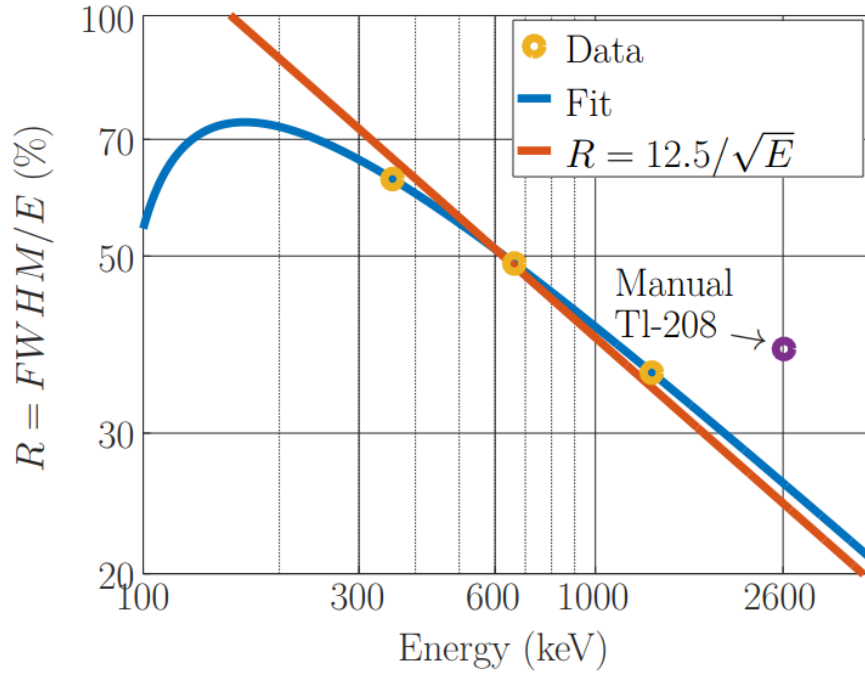
Figure 37. The resolution calibrations obtained from the fits shown in Fig. 35. The purple point from manual ^{208}Tl fitting was not used for this calibration.
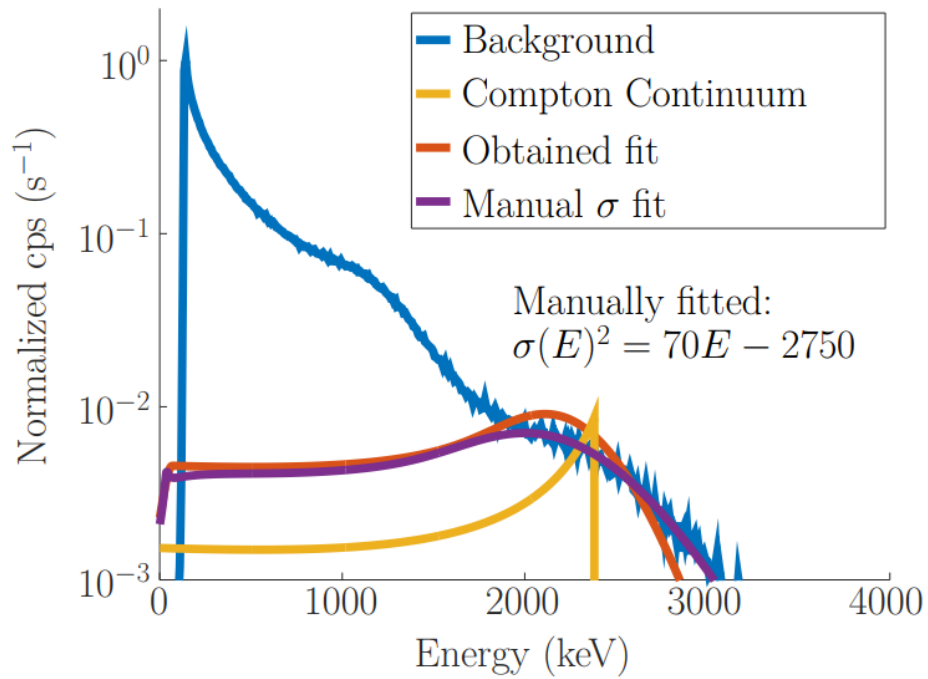
Figure 38. Fits of the ^{208}Tl area in the background spectrum using parameters obtained from the initial fits (Fig. 35) and by manual parameter adjustment.
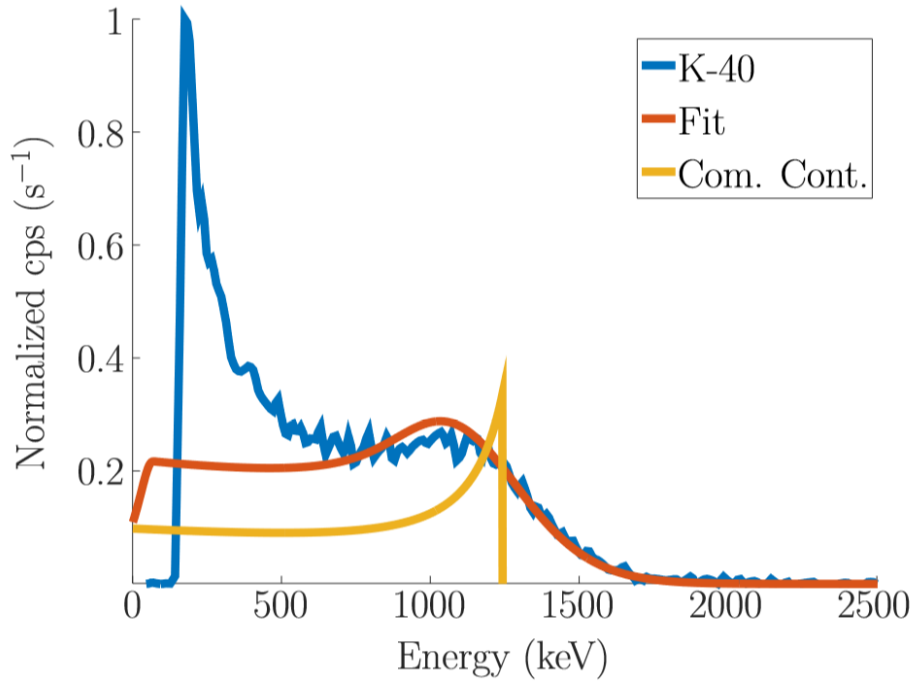
Figure 39. Fit for background subtracted ^{40}K spectrum using parameters from the initial fits (Fig. 35).
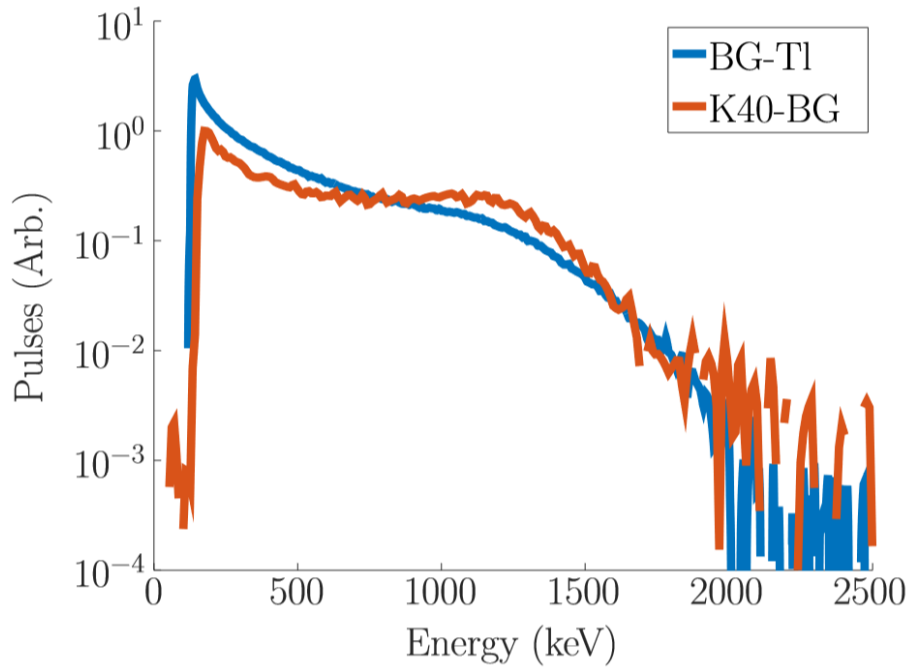
Figure 40. ^{208}Tl-stripped background spectrum (from Fig. 38) and background subtracted ^{40}K spectrum (from Fig. 39)
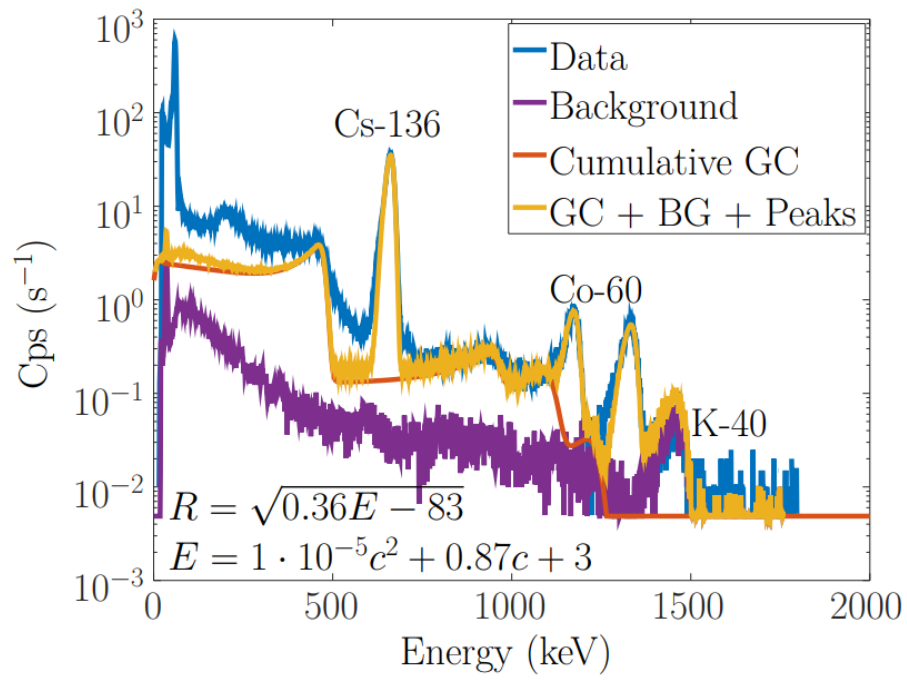
Figure 41. GC-function fitted to multiple sources measured with 1.5" LaBr$_3$.

6 Summary

A commercial PS was analysed. The PS was still uniform showing now significant cracks in Fig. 17 and 18 of Section 5.1. The effects of ageing was visible already with naked eye in a similar old PS (Section 5.2 Fig. 21) and the expectedly short attenuation length of the PS used in this thesis was indeed short, 180 ± 30 mm. Furthermore the Compton edge of 356 keV gamma from ^{133}Ba was calculated to be almost under the static noise line shown in Section 5.3 Fig. 35. All these suggest that the renewal of scintillation material and possibly re-evaluation the PMT of our PS system is near.

Regardless of its condition, the PS inspected in this thesis could be still used for rough nuclide identification using the two-channel method. By adjusting the alarm levels and especially the tolerance for NORM sources the nuisance alarms can be suppressed while maintaining high detectability for non-NORM sources. The possibilities of spectroscopy analysis using numerical fitting method presented in Section 5.3 are promising and could be further refined and implemented to an operational systems.

References

[1] A. Artikov, D. Chokheli, G. Pauletta, and A. Simonenko. The loss of light yield with time in the CDF II scintillation counters. *Nuclear Instruments and Methods in Physics Research Section A: Accelerators, Spectrometers, Detectors and Associated Equipment*, 672:46 – 51, 2012.

[2] James Ely, Richard Kouzes, John Schweppe, Edward Siciliano, Denis Strachan, and Dennis Weier. The use of energy windowing to discriminate snm from norm in radiation portal monitors. *Nuclear Instruments and Methods in Physics Research Section A: Accelerators, Spectrometers, Detectors and Associated Equipment*, 560(2):373 – 387, 2006.

[3] Philip Holm, Kari Peräjärvi, Samu Ristkari, Teemu Siiskonen, and Harri Toivonen. A capture-gated neutron spectrometer for characterization of neutron sources and their shields. *Nuclear Instruments and Methods in Physics Research Section A: Accelerators, Spectrometers, Detectors and Associated Equipment*, 751:48 – 54, 2014.

[4] Chankyu Kim, Hyunjun Yoo, Yewon Kim, Myungkook Moon, Jong Yul Kim, Dong Uk Kang, Daehee Lee, Myung Soo Kim, Minsik Cho, Eunjoong Lee, and Gyuseong Cho. Calculation of gamma spectra in a plastic scintillator for energy calibration and dose computation. *Radiation Protection Dosimetry*, 170(1-4):377–381, 2016.

[5] Chankyu Kim, Hyunjun Yoo, Yewon Kim, Myungkook Moon, Jong Yul Kim, Dong Uk Kang, Daehee Lee, Myung Soo Kim, Minsik Cho, Eunjoong Lee, and Gyuseong Cho. Calculation of gamma spectra in a plastic scintillator for energy calibrationand dose computation. *Radiation Protection Dosimetry*, 170(1-4):377–381, 2016.

[6] G.F. Knoll. *Radiation Detection and Measurement*. John Wiley & Sons, fourth edition, 2010.

[7] N. Kudomi. Energy calibration of plastic scintillators for low energy electrons by using compton scatterings of γ rays. *Nuclear Instruments and Methods in Physics Research Section A: Accelerators, Spectrometers, Detectors and Associated Equipment*, 430(1):96 – 99, 1999.

[8] Brookhaven National Laboratory. National Nuclear Data Center. `https://www.nndc.bnl.gov`. Retrieved: 2017-12-18.

[9] Shelby S. Oakley. Radiation portal monitors: Dhs's fleet is lasting longer than expected, and future acquisitions focus on operational efficiencies. Technical report, U.S. Government Accountability Office, 2016. GAO-17-57.

[10] U.S. Department of Commerce. National Institute of Standards and Technology, NIST. `www.nist.gov/`. Retrieved: 2017-12-18.

[11] K. Roemer, G. Pausch, C. M. Herbach, Y. Kong, R. Lentering, C. Plettner, J. Stein, M. Moszynski, L. Swiderski, and T. Szczesniak. A technique for measuring the energy resolution of low-Z scintillators. In *2009 IEEE Nuclear Science Symposium Conference Record (NSS/MIC)*, pages 6–11, Oct 2009.

[12] State Research Center - Institute for High Energy Physics, IHEP. Block scintillators. `exwww.ihep.ru/scint/`. Retrieved: 2018-04-11.

[13] Lukasz Swiderski, Marek Moszyński, Wiesław Czarnacki, Joanna Iwanowska, Agnieszka Syntfeld-Każuch, Tomasz Szczęśniak, Guntram Pausch, Cristina Plettner, and Katja Roemer. Measurement of Compton edge position in low-Z scintillators. *Radiation Measurements*, 45(3):605 – 607, 2010. Proceedings of the 7th European Conference on Luminescent Detectors and Transformers of Ionizing Radiation (LUMDETR 2009).

[14] E. D. Sword. Humidity-induced damage in polyvinyl toluene and polystyrene plastic scintillator. In *2017 IEEE International Symposium on Technologies for Homeland Security (HST)*, pages 1–4, 2017.

[15] L.P. Ekström S.Y.F. Chu and R.B. Firestone. The Lund/LBNL Nuclear Data Search. `http://nucleardata.nuclear.lu.se/toi`, 1999. Retrieved: 2017-12-18.

[16] Eljen Technology. Scintillator properties. `eljentechnology.com`, 2016. Retrieved: 2017-04-20.

Software

GNU Octave 4.2.1, `octave.org/`
Texmaker 4.5, `xm1math.net/texmaker/`
Maestro, for MCA module

Hardware

A computer

Scintillators:
  Commercial plastic scintillator(s) with a PMT
  $LaBr_3$: Saint-Gobain BrilLanCe 380, 1.5" x 1.5" and 3" x 3"
  PMT base for $LaBr_3$'s: Ortec ScintiPack 296

Nuclear instrumentation modules:
  Inverter: Philips Scientific 740
  MCA: Ortec 927
  Delay: Ortec 427A
  Amplifier: Ortec 572A
  TFA: Canberra 2111
  SCA: Ortec 550
  Gate & Delay: Ortec 416A

A comparator-counter circuit

Appendix

A Calculation methods

A.1 Klein-Nishina reformating

The energy of a Compton scattered gamma is as Eq. (1),

$$E^* = \frac{E}{1 + \frac{E}{m_e c^2}(1 - \cos\theta)} \tag{A.1.1}$$

where E^* is the scattered gamma's energy, E is the initial gamma's energy, $m_e c^2$ is the rest mass of an electron in eV's, and θ is the scattering angle with respect to the initial gamma's direction. By notation $\alpha = E/m_e c^2$ and rearranging the equation we get a relations

$$\frac{E^*}{E} = \frac{1}{1 + \alpha(1 - \cos\theta)} \tag{A.1.2}$$

and

$$\alpha(1 - \cos\theta) = \frac{E}{E^*} - 1 \,. \tag{A.1.3}$$

The Klein-Nishina given by G. F. Knoll [6] is the differential cross section $d\sigma_{\text{KN}}$ with respect to a small scattering solid angle $d\Omega$,

$$\frac{d\sigma_{\text{KN}}}{d\Omega} = Zr_0^2 \left(\frac{1}{1 + \alpha(1 - \cos\theta)}\right)^2 \left(\frac{1 + \cos^2\theta}{2}\right) \left(1 + \frac{\alpha^2(1 - \cos\theta)^2}{(1 + \cos^2\theta)[1 + \alpha(1 - \cos\theta)]}\right) \tag{A.1.4}$$

where $\alpha = E/m_e c^2$, r_0 is the classical electron radius, and Z is the atomic number of the scattering material. For free electrons $Z = 1$. By substituting relations (A.1.2) and (A.1.3) to Eq. (A.1.4) we get another common form of Klein-Nishina equation,

$$
\begin{aligned}
\frac{d\sigma_{\text{KN}}}{d\Omega} &= Zr_0^2 \left(\frac{E^*}{E}\right)^2 \left(1 + \cos^2\theta + (1 + \cos^2\theta)\frac{\alpha^2(1 - \cos\theta)^2}{1 + \cos^2\theta}\frac{E^*}{E}\right)/2 \\
&= Zr_0^2 \left(\frac{E^*}{E}\right)^2 \left(1 + \cos^2\theta + \alpha^2(1 - \cos\theta)^2\frac{E^*}{E}\right)/2 \\
&= Zr_0^2 \left(\frac{E^*}{E}\right)^2 \left(1 + \cos^2\theta + (\frac{E}{E^*} - 1)^2\frac{E^*}{E}\right)/2 \\
&= Zr_0^2 \left(\frac{E^*}{E}\right)^2 \left(1 + \cos^2\theta + ((\frac{E}{E^*})^2 - 2\frac{E}{E^*} + 1)\frac{E^*}{E}\right)/2 \\
&= Zr_0^2 \left(\frac{E^*}{E}\right)^2 \left(-1 + \cos^2\theta + \frac{E}{E^*} + \frac{E^*}{E}\right)/2 \\
&= Zr_0^2 \left(\frac{E^*}{E}\right)^2 \left(\frac{E^*}{E} + \frac{E}{E^*} - \sin^2\theta\right)/2.
\end{aligned}
\tag{A.1.5}
$$

Because we're interested on the probability distribution as a function of the energy disposed to the scattered electrons, we define the energy of the scattered electron $T = E - E^*$, and a variable $S = T/E$. Now

$$
\frac{E^*}{E} = \frac{E - E + E^*}{E} = 1 - \frac{T}{E} = 1 - S.
\tag{A.1.6}
$$

The Eq. (A.1.3) can then be brought to a form

$$
\alpha(1 - \cos\theta) = \frac{1}{1 - S} - 1
\tag{A.1.7}
$$

from where we can solve $\cos^2\theta$ as

$$
\begin{aligned}
\cos^2\theta &= \left(1 - \frac{1}{\alpha(1 - S)} + \frac{1}{\alpha}\right)^2 \\
&= 1 + \frac{1}{\alpha^2(1 - S)^2} + \frac{1}{\alpha^2} - \frac{2}{\alpha(1 - S)} + \frac{2}{\alpha} - \frac{2}{\alpha^2(1 - S)}.
\end{aligned}
\tag{A.1.8}
$$

We also need the derivative

$$
\begin{aligned}
\frac{d(\cos\theta)}{dT} &= \frac{d}{dT}\left(1 - \frac{1}{\alpha(1 - S)} + \frac{1}{\alpha}\right) \\
&= \frac{d}{dT}\left(1 - \frac{E}{\alpha(E - T)} + \frac{1}{\alpha}\right) \\
&= \frac{E}{\alpha(E - T)^2} \\
&= \frac{1}{E\alpha}\frac{1}{(1 - S)}^2 \\
&= \frac{1}{m_e c^2 \alpha^2}\left(\frac{E}{E^*}\right)^2.
\end{aligned}
\tag{A.1.9}
$$

As the last intermediate step we will use the assumption that the Compton scattering process is independent of the azimuthal angle ϕ and eliminate it from the Klein-Nishina differential. We start by the definition of total cross section:

$$
\begin{aligned}
\sigma_{\mathrm{KN}} &= \oint_{\Omega} \frac{d\sigma_{\mathrm{KN}}}{d\Omega} d\Omega \\
&= \int_{\phi} \int_{\theta} \frac{d\sigma_{\mathrm{KN}}}{d\Omega} \sin\theta d\theta d\phi\,.
\end{aligned}
\tag{A.1.10}
$$

We define a variable $u = \cos\theta$. Now $du = du/d\theta \cdot d\theta = -\sin\theta d\theta$. Because u is strictly decreasing as θ increases, the boundaries of u need to be swapped introducing a negative sign for the integral. Substituting u into Eq. A.1.10 we get

$$
\sigma_{\mathrm{KN}} = -\int_{\phi} \int_{u} \frac{d\sigma_{\mathrm{KN}}}{d\Omega} (-du) d\phi\,.
\tag{A.1.11}
$$

By differentiating both sides with respect to u and applying the fundamental theorem of calculus we get

$$
\frac{d\sigma_{\mathrm{KN}}}{d(\cos\theta)} = \frac{d\sigma_{\mathrm{KN}}}{du} = \int_{\phi} \frac{d\sigma_{\mathrm{KN}}}{d\Omega} d\phi = 2\pi \frac{d\sigma_{\mathrm{KN}}}{d\Omega}\,.
\tag{A.1.12}
$$

We can now form our electron's energy distribution by applying chain rule to Eq. (A.1.5) and substituting the Eq. (A.1.6), (A.1.7), (A.1.8), (A.1.9), and (A.1.12) as

such:

$$
\begin{aligned}
\frac{d\sigma_{\mathrm{KN}}}{dT} &= \frac{d\sigma_{\mathrm{KN}}}{d(\cos\theta)} \cdot \frac{d(\cos\theta)}{dT} \\
&= 2\pi \frac{d\sigma_{\mathrm{KN}}}{d\Omega} \cdot \frac{1}{m_e c^2 \alpha^2} \left(\frac{E}{E^*}\right)^2 \\
&= \frac{2\pi}{m_e c^2 \alpha^2} \left(\frac{E}{E^*}\right)^2 \cdot Z r_0^2 \left(\frac{E^*}{E}\right)^2 \left(\frac{E^*}{E} + \frac{E}{E^*} - \sin^2\theta\right)/2 \\
&= \underbrace{\frac{Z r_0^2 \pi}{m_e c^2}}_{\doteq C} \cdot \frac{1}{\alpha} \left(\frac{E^*}{E} + \frac{E}{E^*} - 1 + \cos^2\theta\right) \\
&= C \cdot \frac{1}{\alpha^2} \\
&\quad \times \left(1 - S + \frac{1}{1-S} - 1 + \left(1 + \frac{1}{\alpha^2(1-S)^2} + \frac{1}{\alpha^2} - \frac{2}{\alpha(1-S)} + \frac{2}{\alpha} - \frac{2}{\alpha^2(1-S)}\right)\right) \\
&= C \cdot \frac{1}{\alpha^2} \left(\underbrace{-S + \frac{1}{1-S} + 1}_{} \underbrace{- \frac{2}{\alpha(1-S)} + \frac{2}{\alpha}}_{} + \underbrace{\frac{1}{\alpha^2(1-S)^2} + \frac{1}{\alpha^2} - \frac{2}{\alpha^2(1-S)}}_{}\right) \\
&= C \cdot \frac{1}{\alpha^2} \left(\frac{-S(1-S) + 1 + (1-S)}{1-S} + \frac{-2 + 2(1-S)}{\alpha(1-S)} + \frac{1 + (1-S)^2 - 2(1-S)}{\alpha^2(1-S)^2}\right) \\
&= C \cdot \frac{1}{\alpha^2} \left(\frac{S^2 + (-1-1)S + (1+1)}{1-S} + \frac{-2S}{\alpha(1-S)} + \frac{S^2 + (-2+2)S + (1+1-2)}{\alpha^2(1-S)^2}\right) \\
&= C \cdot \frac{1}{\alpha^2} \left(\frac{S^2 - 2S + 2}{1-S} + \frac{-2S}{\alpha(1-S)} + \frac{S^2}{\alpha^2(1-S)^2}\right) \\
&= C \cdot \frac{1}{\alpha^2} \left(\frac{2(1-S)}{1-S} + \frac{S^2}{1-S} + \frac{-2S}{\alpha(1-S)} + \frac{S^2}{\alpha^2(1-S)^2}\right) \\
&= C \cdot \frac{1}{\alpha^2} \left(2 + \frac{S}{1-S}\left(S - \frac{2}{\alpha}\right) + \frac{S^2}{\alpha^2(1-S)^2}\right).
\end{aligned}
$$

$$(\mathrm{A.1.13})$$

As Eq. (A.1.13) is directly proportional to the probability for an electron to have kinetic energy T after a gamma with energy α scatters from it, the constant C can simply be used as a normalization coefficient.

A.2 Exponential fitting to coincidence mean locations

The function modelling the dependencies between the mean channel μ and the distance d from source to a point near PMT was presented as

$$\mu = Ae^{-d/\lambda} + B$$

where A, B and λ are parameters to evaluate by fitting. The uncertainties are used as weights for the mean values in the fitting process. Since we have significant uncertainties in both distances $\delta d = \sqrt{500}$ mm and mean values $\delta\mu = 0.03\mu$ in Section 5.2.3 these need to be combined to $\delta\mu_{tot}$. Using the propagation of uncertainties we get

$$\delta\mu_{tot} = \sqrt{\left(\frac{\partial\mu}{\partial\mu}\right)^2 \delta\mu^2 + \left(\frac{\partial\mu}{\partial d}\right)^2 \delta d^2}$$
$$= \sqrt{\delta\mu^2 + \left(-\frac{A}{\lambda}e^{-d/\lambda}\right)^2 \delta d^2}\,.$$

Because the parameters A and λ are still to be evaluated this equation cannot be analytically solved yet. Instead, we form an iterative process for approximation of the partial derivative, or the slope, $\partial\mu/\partial d$. In the first step a fit that takes into account no uncertainties is formed. The parameters gained this way are used in the second step to approximate the slope $(-A/\lambda)e^{-d/\lambda}$.

After attaining the slope approximation the distance uncertainty it was realized to be less than 20% of the uncertainty of the mean channel μ. Furthermore, the values for the parameters A, B and μ all changed less than 2% from the first step which is less than relative uncertainties of parameter μ. The standard errors of the final parameter values also changed only minorly.

Octave code used for the fitting:

```
% Distances in column vector 'd', means in 'mu'.
pkg load optim
dd = 500
dmu = 0.03
[_ p1 _ _ _ cov1] = leasqr(d, mu, [30 500 40],
  @(x,p)(p(1)*exp(-x./p(2))+p(3)));
[_ p2 _ _ _ cov2] = leasqr(d, mu, [30 500 40],
  @(x,p)(p(1)*exp(-x./p(2))+p(3)), [], [], ...
  1./sqrt(sumsq( ...
  [dmu*mu dd*ptemp(1)./ptemp(2).*exp(-d./ptemp(2))], 2)));

% [A lam B] = p2
% variance{n} = vec(sqrt(diag(cov2)));
```
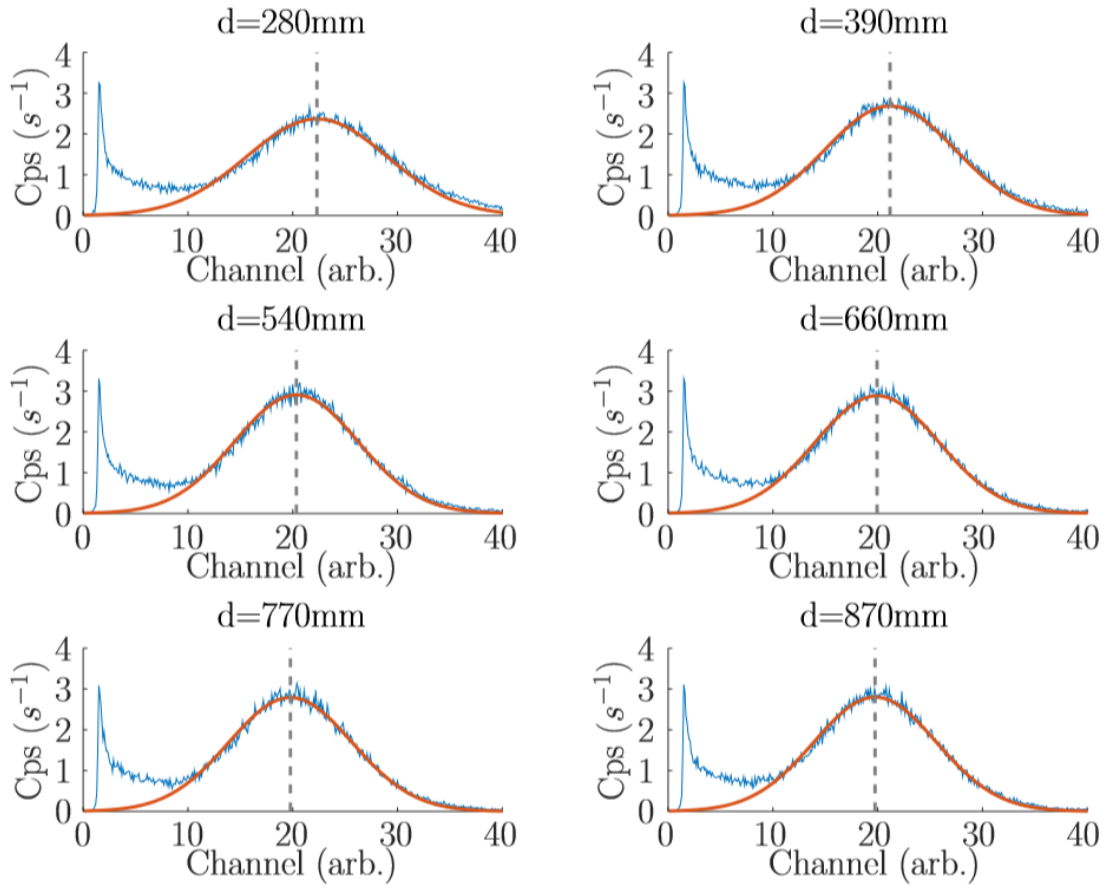
B   Spectra and data from the attenuation length measurements
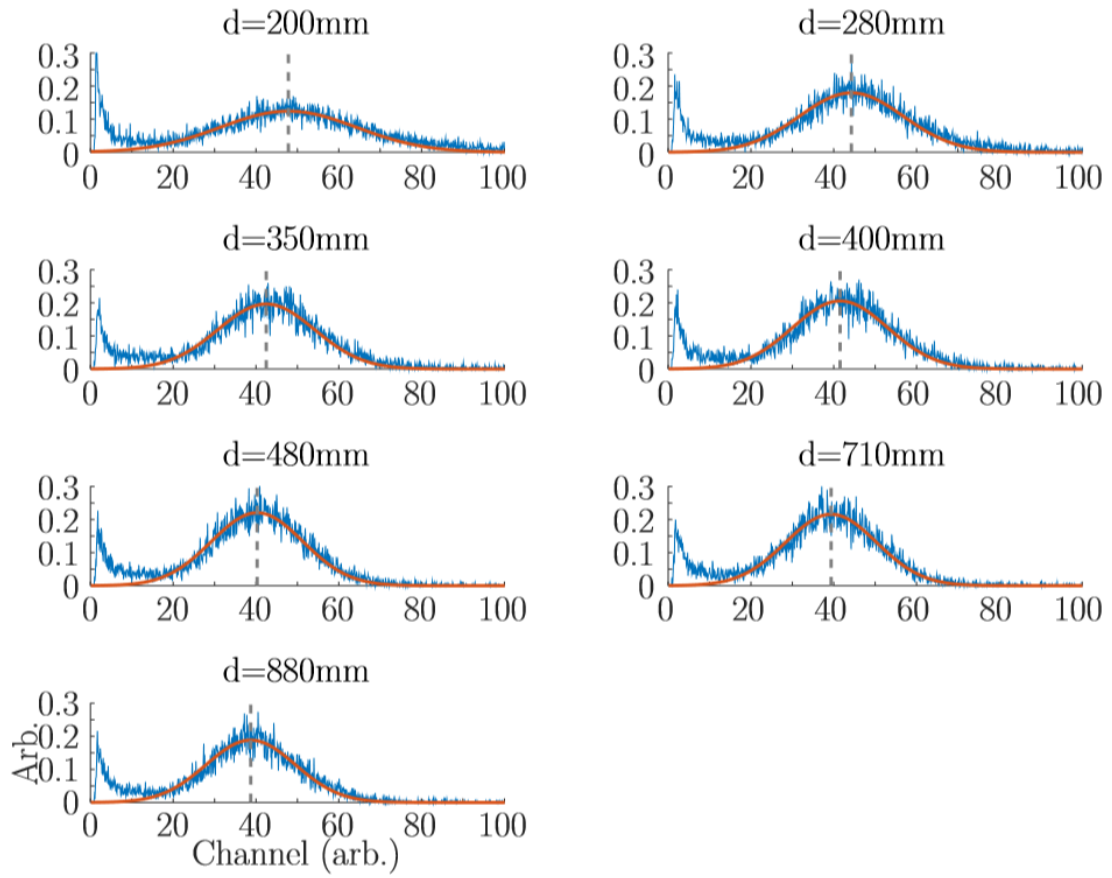
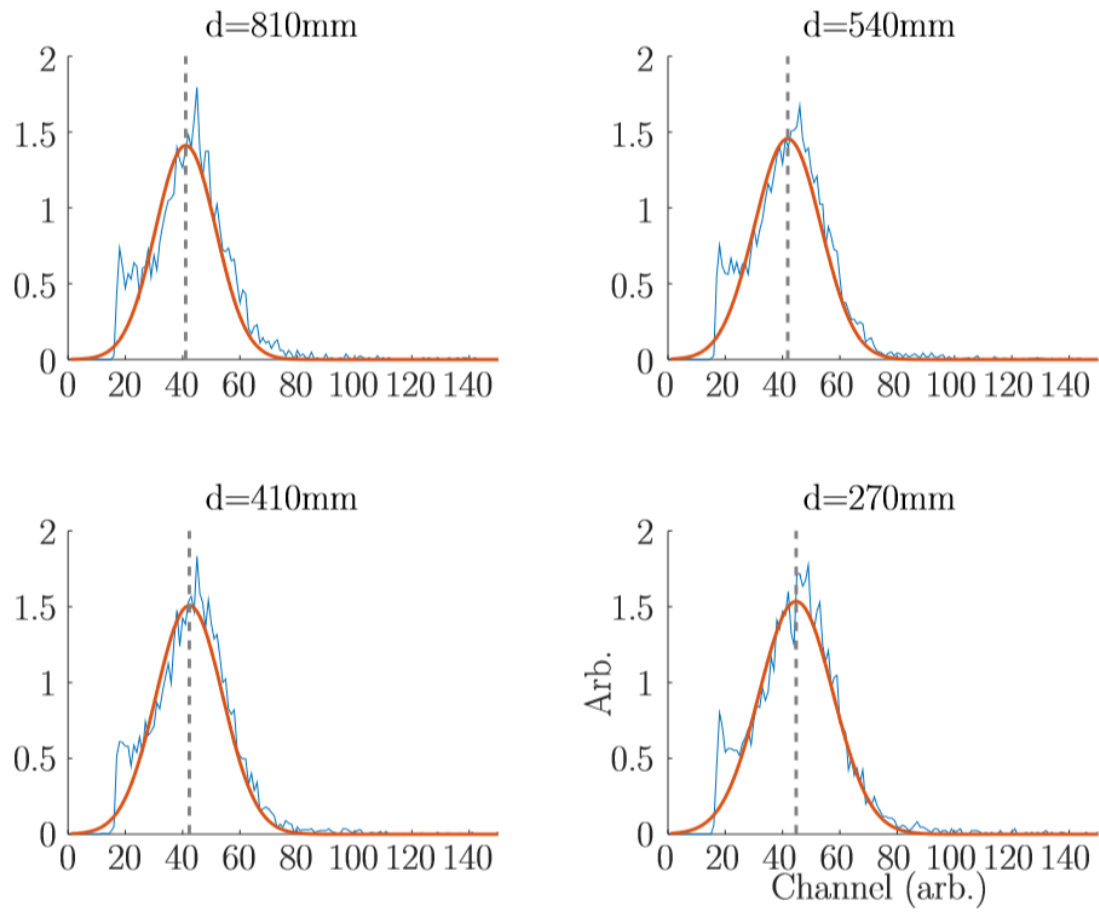**Figure 42.** The spectra measured from different distances using the 1.5" LaBr$_3$.
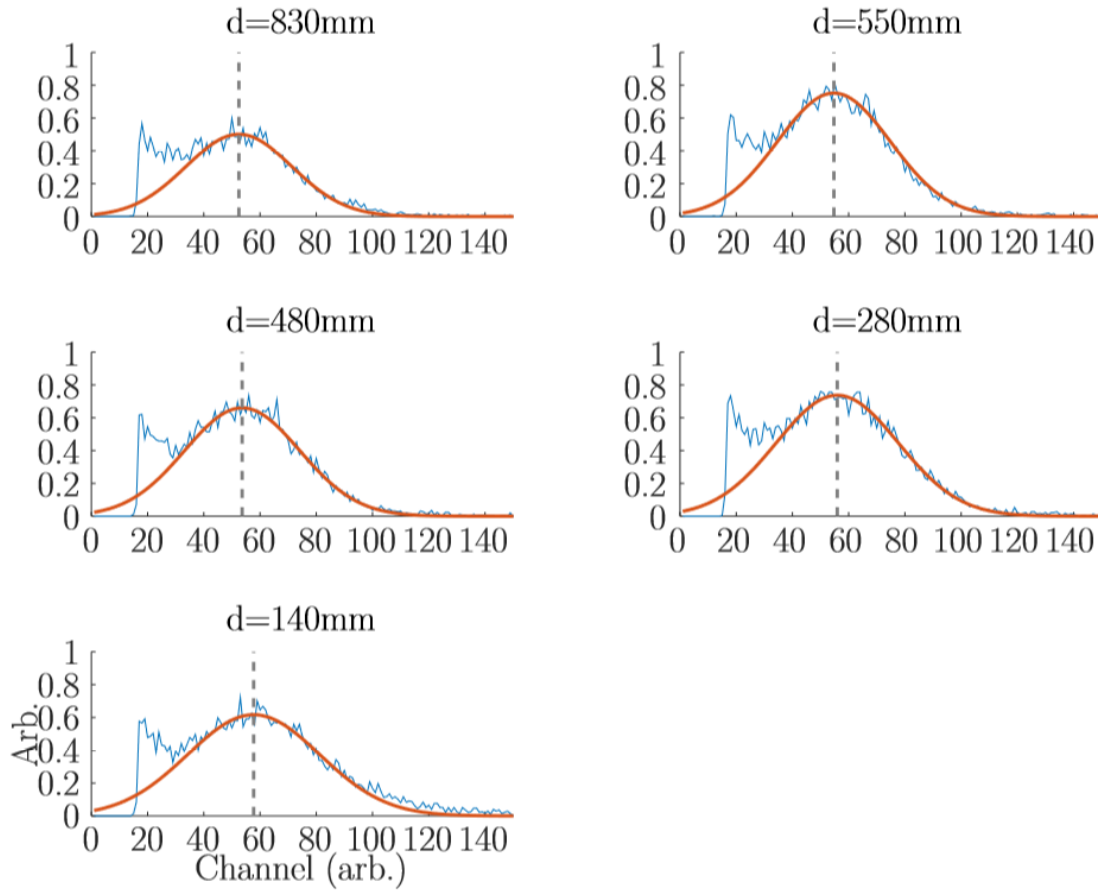
Figure 43. The spectra measured from different distances using the 3" LaBr$_3$.

Figure 44. The spectra measured from different distances using the 1.5" LaBr$_3$ on field from the first PS.

Figure 45. The spectra measured from different distances using the 1.5" LaBr$_3$ on field from the second PS.

Table 4. Means and FWHMs gathered from coincidence measurement spectra presented in Appendix B. In Field measurements the 1.5" LaBr$_3$ was used.

Lab 1.5"

d (mm)	μ (Arb.)	$FWHM$ (Arb.)
200	47.82	38.8
280	44.25	29.56
350	42.48	27.5
400	41.53	27.12
480	40.28	26.01
710	39.36	25.88
880	38.73	25.35

Lab 3"

d (mm)	μ (Arb.)	$FWHM$ (Arb.)
280	56.130	38.920
390	53.620	35.730
540	51.470	33.830
660	50.520	33.820
770	50.310	33.630
870	50.110	33.870

Field 1

d (mm)	μ (Arb.)	$FWHM$ (Arb.)
270	44.740	30.280
410	42.340	27.370
540	41.810	27.290
810	41.080	24.880

Field 2

d (mm)	μ (Arb.)	$FWHM$ (Arb.)
140	57.730	55.310
280	55.940	51.130
480	53.640	48.140
550	54.740	47.350
830	52.480	44.460

C GC fitting Octave script

All energies are in keV. Run the script in a same directory with the data file (here called 'data.txt') which contains the measurement data in independent columns, here as [Ba Cs Co] without headers. Requires a package optim.

```
%% User parameters:
E = (1:2000)'; % Energy range
th = pi*linspace(0,1,1000); % Scattering angles
E0 = [356 662 1333]; % Initial gamma energies
roi = [24 48 , 40 110 , 80 200]'; % Region of interest for the fits, in channels
fname = 'data.txt'; % File containing the data
% Initial quesses for the fit parameters:
% [[energy calibration parameters] [variance parameters] [y-scaling per spectrum]]
Eparms = 1:3;
varparms = 4:5;
yparm = 6;
p0 = vec([[0 8 0] [25 0] [0.06 0.6 2]]');
%% Fitting process
% Loading data.
% In data file, each column is a measurement: Ba, Cs, Co.
cps = [load(fname)];
cps = cps./max(cps); % Normalize for aesthetic reasons
% Append zeros to match the energy range length.
cps = [cps ; zeros(size(E,1)-size(cps,1), size(cps,2))];
mc2 = 511;
Es = comptonEnergy(E0, th); % Scattered gamma energy
Ec = E0 .- Es; % Electron energy disposed by the scattered gamma
% Klein-Nishina, KN
a = E0/mc2;
s = Ec/E0;
kn = @(a,s)(1./(a.^2) .* (2 + s.^2./(a.^2.*(1.-s).^2) + s./(1.-s) .*(s .-2./a)));
kn_temp = kn(a,s);
% Interpolating Klein-Nishina values from Ec to E,
%    since Ec is not equally spaced (even though 'th' is).
%    Beyond scope values are set to 0.
for n=1:numel(E0)
    P(:,n) = interp1(Ec(:,n), kn_temp(:,n), E, 0);
endfor
%% Gaussian distribution.
function ret = d(x, x0, sr)
    ret = 1./sqrt(2*pi*abs(polyval(sr,x0))).*exp(-(x.-x0).^2./(2*abs(polyval(sr,x0))));
endfunction
% Convolution of and Compton continuum 'P' Gaussian distribution '@d'.
% Returns a vertical vector of size E.
% Integration horizontally, range: E0.
% (f * g)(E): f = KN(E0>).*Gauss(E0>,E^)
C = @(E, E0, sr, P)(trapz(E0, P'.*d(E0', E, sr), 2));
% Region of interest for the fits, ROI, in channels
x = {(roi(1):roi(2))' ; (roi(3):roi(4))' ; (roi(5):roi(6))'};
% Fitting the functions. Uses 'leasqr' function from package 'optim'.
pkg load optim
[f, p, in, iter, corp, covp, covr, stdresid, Z, r2]  = leasqr( ...
  roi, ...
  [cps(x{1},1) ; cps(x{2},2) ; cps(x{3},3)], ...
  p0, ...
  @(roi, p)( ...
    [C(polyval(p(Eparms),[roi(1):roi(2)]'), E, p(varparms), P(:,1))*p(yparm+0) ; ... % Ba fit
     C(polyval(p(Eparms),[roi(3):roi(4)]'), E, p(varparms), P(:,2))*p(yparm+1) ; ... % Cs fit
     C(polyval(p(Eparms),[roi(5):roi(6)]'), E, p(varparms), P(:,3))*p(yparm+2) ; ... % Co fit
 ] ));
for n = 1:numel(E0)
    y(:,n) = C(E, E, p(varparms), P(:,n))*p(yparm+n-1); % 'y' holds the fitted GC's for each spectrum
endfor
xcps = polyval(p(Eparms), E); % Energy calibrated x-values for 'cps'
plot(xcps, cps, E, y)
```